Experimental Investigation of the Secondary and Backscatter Electron Emission from New Spacecraft Surface Materials

Millan F. Diaz-Aguado, *Member, IEEE*, John W. Bonnell, Stuart D. Bale, Justin Christensen, Phillip Lundgreen, Jordan Lee, JR Dennison, *Member, IEEE*, Justin Dekany, Brian Wood and Mike Gruntman

***Abstract*— The emission of Secondary (SE) and Backscattered Electrons (BSE) influences spacecraft surface potentials and the surrounding plasma. Spacecraft potentials are determined by the current balance of arriving and departing electrons, ions, and photons. SE and BSE often play a significant role in that current balance, and so knowledge of the SE and BSE fluxes from exposed surfaces is crucial in determining those floating potentials, especially in eclipse. Modern spacecrafts use new materials for which secondary emission properties have been unavailable, leading to uncertainties in the surface charging of and plasma environment around those spacecrafts. In this work, the total electron yield, SE yield and BSE yield were measured for Niobium-C103 alloy, Molybdenum TZM alloy, Tantalum Tungsten alloy, Elgiloy, graphite lubricant (DAG 213) and Titanium Nitride. The surface properties of Tungsten were also measured for comparison with past test data. The materials were readied as spacecraft flight materials and temperature treated ("annealed") to predicted peak flight temperatures. The yield properties for 10eV-5keV incident electron energies for all samples were measured. Both unannealed and annealed states were tested, except DAG 213, which was only tested annealed. Three-parameter and four-parameter models was used to fit the BSE and SE yield data, respectively. The emitted electron energy distributions are also obtained and fit with a Chung-Everhart model for SE and a Gaussian function for BSE. The SE and BSE currents densities were calculated for different ambient plasma conditions, including at GEO, in the magnetosheath, and solar wind at heliocentric distances from 1AU to 9.5 solar radii (0.044 AU) away from the Sun. For ready reference, the normalized primary electron, SE and BSE current densities versus ambient electron temperature were computed and plotted from 1eV to 8keV.**

***Index Terms*— Backscattered Electron Yield, Secondary Electron Current, Secondary Electron Yield, Spacecraft Charging.**

I. Introduction

The plasma environment can have significant and detrimental effects on spacecraft (SC) operations [5-11], affecting the plasma measurements and causing surface charging events. Incident electrons on a surface result in secondary electrons (SE) and backscattered electrons (BSE) emission. BSE are electrons originating from the external environment which scatter with the material, and eventually reverse direction and backscatter out of the material. SE emitted electrons that originate within the material, are excited by collisions of incident electrons, and escape from a surface. SE and BSE are some of the most important surface charging mechanisms [5, 12-15], which also include photoemission and ion SE.

Large potential differentials caused by differential charging from SE and BSE have caused anomalies on spacecraft (SC) and their instruments [12,19, 16, 17], but there is still some debate on how the electron fluxes cause SC charging events [18]. Based on results from the Spacecraft Charging at High Altitudes (SCATHA) mission there are several studies [8, 19, 20] that show what range of ambient electron energies cause spacecraft charging at GEO. All the studies differ in their detailed conclusions, but they agreed that the ambient electron temperature must peak above 3keV for SE and BSE to play a significant role in SC charging.

SE and BSE yield (SEY and BSEY) as a function of incident electron energy are available both in the literature and in the simulation packages (NASCAP and SPIS) [21, 22], but myriad

This research was supported in part by NASA contract # NNN06AA01C

M.F. Diaz-Aguado is with SRI International, Menlo Park, CA 94025, USA (e-mail: millan.diaz-aguado@sri.com)

J. W. Bonnell is with Space Sciences Laboratory, University of California, Berkeley, CA, 94720, USA (e-mail: jwbonnell@berkeley.edu)

S. D. Bale is with Space Sciences Laboratory, University of California, Berkeley, CA, 94720, USA (e-mail: bale@ssl.berkeley.edu)

J. Christensen is with Physics Department, Utah State University, Logan, UT, 84322, USA (e-mail: spyder23@comcast.net)

J. Lee is with Physics Department, Utah State University, Logan, UT, 84322, USA (e-mail: jordan.lee@aggiemail.usu.edu)

P. Lundgreen, is with Physics Department, Utah State University, Logan, UT, 84322, USA (e-mail: phillip.lundgreen@aggiemail.usu.edu)

JR Dennison is with Physics Department, Utah State University, Logan, UT, 84322, USA (e-mail: jr.dennison@usu.edu)

J. Delany is with Physics Departmanet, Utah State University, Logan, UT, 84322, USA (e-mail: jdekany.phyx@gmail.com)

B. Wood is with Physics Department, Utah State University, Logan, UT, 84322, USA (e-mail: brian.wood314@gmail.com)

Mike Gruntman is with Astronautical Engineering Department, University of Southern California, Los Angeles, CA, 90089 (mikeg@usc.edu)

new SC materials have been introduced and used in the last decade for which no data is available, motivating this study.

This research studied the effects of incident electron with energies up to 5keV for Ta-W, TZM, TiN and DAG213. It also measured Nb-C103, Elgiloy and W to 30keV. Tungsten has been studied extensively [1] and was chosen as a benchmark material with similar refractory properties for these studies. The other new untested materials are being utilized on Langmuir probes used to measure density and potential variations in the plasma. Current missions that include these probes as part of their instrument suite include Time History Events and Macroscale Interactions during Substorms (THEMIS) [23], Van Allen Probes [24], Cassini [25], Mars Atmosphere and Volatiles Evolution (MAVEN) [26], MMS (Magnetospheric Multiscale) [27], Solar Orbiter [28] and Solar Probe Plus (SPP) now Parker Solar Probe (PSP) [29].

During the mission of PSP, the SC is traveling from the Earth to 9.5 solar radii away from the Sun. Most of the bus will be protected by a carbon-carbon and alumina heat shield, except two instruments which are exposed to the full solar flux (the FIELDS antennas and the SWEAP faraday cup). The SC will orbit around the Sun, slowly decreasing its periapsis, and slowly increasing temperature of the antennas, faraday cup and shield, which are mainly composed of Nb-C103 and TZM, with Ta-W as the backup material for Nb-C103. The heating experienced by the surfaces will anneal them, which may change the SE yield and the energy distribution of emitted electrons and thus impact sheath properties. Any change in the SEY or BSEY also influences the corresponding current, and thus SC charging and floating potential.

Other recent or future missions also make use of novel untested materials: The ESA Solar Orbiter mission will also study the Sun but at a higher altitude (0.25 AU) than PSP, using Elgiloy for their probes. MAVEN, a mission to study Mars, and Cassini, mission to study Saturn, uses Langmuir probes coated with TiN. THEMIS, Van Allen Probes and MMS studied the magnetosphere and Van Allen belts with highly elliptical orbits. These SC had DAG 213 on their probes.

Studying the SE and BSE yields of these new materials will help in modeling SC charging, specifically in software packages like NASCAP and SPIS. In order to measure the effects of annealing, the samples were characterized before and after exposure to expected flight temperatures. This study did not include SE emission testing at the peak temperatures.

Because SE occurs mainly near the surface, SE yields are sensitive to surface contamination [9, 30, 31]. In order to best capture this effect for these materials in their flight configuration, the samples were prepared similarly to flight materials using cleaning processes described in the experimental section.

Once cleaned, the samples were then exposed to an electron beam at normal incidence. The Total Electron Yield (TEY) and BSE yields (BSEY) were measured, and SEY were obtained through subtraction. All the samples were then heat-treated at temperatures similar to maximum flight temperatures to anneal them. The yield measurements were then repeated for all samples, except for DAG 213, to search for differences in the samples, and its effects on SEY and BSEY.

The details of the experimental setup and test results are described below. First, the experimental setup is explained in the Electron Emission Test (EET) Chamber at Utah State University (USU)[32], followed by the theoretical models used[15]. Second, the experimental results are shown for SEY, BSEY and TSEY for the materials tested, including the theoretical fits. The SE and BSE energy distribution are also shown. Subsequently, the SE and BSE current densities are calculated for different ambient plasma, ending with a conclusion.

II. Experimental

All tests were conducted at room temperature in the EET Chamber by USU Materials Physics Group [1, 32]. The test system uses a fully encased hemispherical grid retarding field analyzer (HGRFA)[33]. The yield measurements were made using 10 electron beam pulses per beam energy (3μs for low incident electron energies and 30μs for high incident electron energies). The biased hemispheres capture the emitted electrons. The HGRFA detector is capable of measuring yields within +/-2% accuracy. By biasing the retarding grid to 0V, the total yield is measured by detecting all electrons. Biasing the retarding grid to -50V allows for only the BSE to reach the detector. The ratio between the incident and emitted charges were then integrated to obtain the Total Electron Yield (TEY) and BSEY.

The SEY are determined by subtracting the BSEY from the TEY. The SE emission spectra was determined with the same HGFRA by scanning the voltage of the retarding grid through a range of voltages. The emission spectra were determined only for an incidence electron energy of 53eV, to be able to distinguish the SE at low energies with the BSE which have similar energies as the incoming electrons. It is assumed that the SE spectra will be similar for all incident energy electrons, and the rough validity of this assumption has been shown experimentally in [33, 34], and theoretically by Chung and Everhart [35]

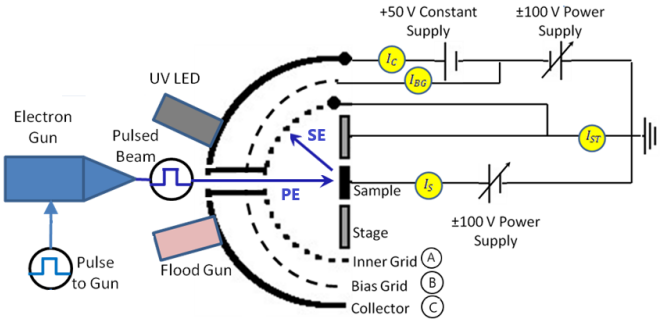

Fig. 1 Schematic of the hemispherical grid retarding field analyzer (HGRFA), with the ammeters (I), ground and voltage biases[1].

TABLE I
MATERIALS PROPERTIES

Sample	Composition	Surface Contamination	Surface Roughness (nm)	Density, ρ_m (g-cm^{-3})	Mean Atomic Number, $\bar{Z}$	Mean Atomic Weight, $\overline{M_A}$	Work Function, ϕ (eV)
W	W (99.98%)	C(5%), O(1%)	≤0.2	19.3	74	183.85	4.55
Nb-C103	Nb(89%), Hf(10%), Ti(1%)	C(8%), O(2%), Rb(2%)	≤0.2	8.85	43.91	101.02	4.1*
TiN	Ti(77%), N(23%)	C(3%)	≤0.1	5.22	14.5	30.94	4.2
Ta-W 10%	Ta(90%), W(10%)	C(5%), O(1%), Fe(0.1%)	≤0.1	16.9	73.1	181.20	4.2*
TZM	Mo(99.3%), Ti(~0.5%), Zr(~0.08%)	C(5%), O(2%)	≤0.5	10.3	42.0	95.94	4.3*
Elgiloy	Co (40±1%), Cr (20±1%), Ni (15±1%), Fe (~15%), Mo (7±1%), Mn (2±0.5%), Si ~1.2%	C(3%), O(3%)	≤0.5	8.30	27.28	59.25	4.3*
DAG-213	Graphite (~10%) / bisphenol epoxy resin $(C_{18}H_{18}O_3)_n$ (~90%) composite	none <0.1%	≤1	0.98	3.77	7.07	~4.7 (epoxy band gap)

* Work functions for alloys are found with a Vegard-like approach, if not specifically available in the literature, using values in [4]

Figure 1 shows a schematic of the HGRFA hemispheres and sample setup [36], where A is the collector, B is biased grid used to discriminate electron energies coming from the sample, and C inner grid used to provide the uniform electric field and shield from unwanted edge effects. The HGRFA resolution is ~2 eV, with additional contributions from the thermal spread of electron sources and electronics for an estimated instrument resolution of ~2.4±0.2 eV. Figure 2 shows an image of the HGRFA and the rotating sample holder inside the EET chamber.

The tungsten sample is a high purity bulk refractory material. Nb C-103 niobium sample is a highly refractory Nb-Hf-Ti alloy typically used in aerospace components and other high temperature environments. TiN is an extremely hard high temperature ceramic material, often used as a coating on metals; this sample was a 2 µm N thick coating on a Ti substrate. The Ta-W sample is a bulk Ta refractory material with ~10% W alloying. Molybdenum TZM is a standard Mo alloy, used in applications that require high strength and creep resistance at elevated temperatures. Elgiloy® is a high temperature non-magnetic Co-Cr-Ni-Mo alloy. DAG 213® is a thermosetting resin-bonded graphic dry film lubricant coating formulated from processed microcrystalline graphite and epoxy resin, often used in space applications as a black thermal control material. Relevant properties of the materials are listed in Table-I.

The samples were treated similarly to materials used during flight missions. First the samples were cut to fit the holder. An ultrasonic methanol bath was then used to clean the surfaces. Immediately afterwards, the samples were baked-out at ~373K for >48 hours. prior to all yield measurements to minimize absorbed water and volatile contaminates. Finally, the samples were stored in a nitrogen glove box until placed inside the EET chamber which was pumped down to 10^{-7} torr.

Surface morphology studied with scanning electron microscopy (SEM) found smooth (though not atomically smooth) surfaces with vertical features less than ½ µm high

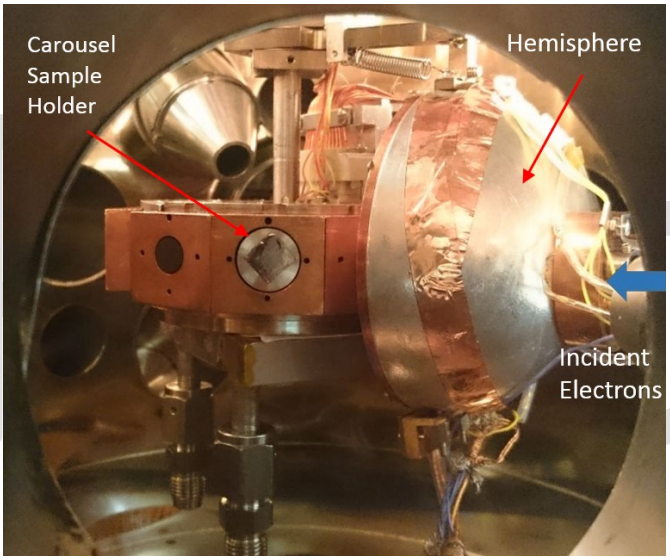

Fig. 2 Image of the HGRFA Hemisphere and Carrousel Sample Holder. The blue arrow indicates the direction of electrons passing through the HGRFA and incident on an electrically isolated sample mounted in a sample carousel sample block.

(except for DAG 213®) (see Table-I). W, TZM, and DAG 213® had ~2-10 µm wide irregular patches; Nb-C103, TiN, Ta-W, and Elgiloy exhibited additional striations from machining or polishing. These rough surfaces may supress the electron yields somewhat, but are not expected to have large effects (except for DAG-213), since the height-to-lateral aspect ratio is typically less than 10% to 50%. Energy Dispersive X-Ray Spectroscopy (EDS) analysis (see Table-I) confirmed the alloy composition, with other contaminants noted in Table-I. All materials had C and O surface contamination evident, suggesting thin organic contamination layers; other contaminates were often contentrated in particulates. Contamintion, especially organic layers or oxide layers, can

TABLE II
SE YIELD PARAMETERS

Sample	δ_{max}	$\left[\frac{\delta^a_{max}-\delta^u_{max}}{\delta^u_{max}}\right]$ * (%)	E_{SEmax} (eV)	$\left[\frac{\Delta E^a_{SEmax}-\Delta E^u_{SEmax}}{\Delta E^u_{SEmax}}\right]$ * (%)	n	$\left[\frac{n^a-n^u}{n^u}\right]$ * (%)	m	$\left[\frac{m^a-m^u}{m^u}\right]$ * (%)	E_1 (eV)	E_2 (keV)	r_{max}
W Unannealed	1.50±0.1	***13%***	230±30	***52%***	1.41±0.08	8%	0.60±0.07	-12%	35±1	1.10±0.1	1.23±0.7
W (1200°C)	1.70±0.1		350±50		1.52±0.06		0.53±0.05		34±1	2.20±0.1	1.25±0.6
Nb-C1O3 Unann.	1.80±0.1	***11%***	300±30	-11%	1.53±0.04	2%	0.46±0.02	-7%	43±2	1.70±0.1	1.23±0.5
Nb-C1O3(1200°C)	2.00±0.1		270±50		1.56±0.04		0.43±0.03		34±2	1.62±0.1	1.33±0.5
TiN Unannealed	2.30±0.1	2%	260±30	-4%	1.64±0.04	1%	0.41±0.03	0%	27±1	1.72±0.07	1.12±0.5
TiN (180°C)	2.35±0.08		250±30		1.65±0.02		0.41±0.01		27±1	1.73±0.07	1.12±0.3
Ta-W 10% Unann.	2.30±0.1	0%	260±30	8%	1.47±0.06	1%	0.44±0.05	5%	18±1	2.9±0.1	1.47±0.7
Ta-W (1200°C)	2.30±0.07		280±30		1.48±0.03		0.46±0.02		23±1	3.0±0.1	1.36±0.5
TZM Unannealed	2.20±0.05	0%	240±30	***17%***	1.59 ±0.06	-3%	0.35±0.1	***37%***	38±1	2.1±0.1	1.79±0.8
TZM (1200°C)	2.20±0.05		280±10		1.54 ±0.02		0.48±0.02		23±1	2.3±0.1	1.30±0.4
Elgiloy Unann.	1.90±0.1	***11%***	300±50	20%	1.62±0.06	1%	0.49±0.04	-8%	33±2	1.60±0.1	1.07±0.5
Elgiloy (800°C)	2.10±0.1		360±30		1.63±0.04		0.45±0.03		36±2	2.07±0.1	1.14±0.5
DAG 213 (180°C)	2.00±0.05	NA	240±50	NA	1.60±0.04	NA	0.45±0.03	NA	33±1	1.45±0.07	1.20±0.6

* Values greater than uncertainties in italics

have significant effects on electron yields which are difficult to predict.

After initial testing, the materials tested were annealed by exposure to temperatures experienced during realistic flight: Nb-C103, TZM and W were annealed at 1473K (1200°C), Elgiloy was annealed at 1073K (800°C) and DAG 213 and TiN were annealed at 423K(180°C). All materials were annealed in a vacuum furnace in a quartz tube at $<10^{-3}$ Pa to avoid oxidation. Such annealing or flight exposure could be expected to remove contamination or smooth the surfaces[37].

Figure 3 shows the electron range for the materials studied here, as well as that of amorphous graphitic carbon for comparison. Ranges were calculated using methods detailed in Wilson [2, 3].

III. THEORETICAL MODELS

The data obtained by the lab experiments were fitted parametrically with well-established theoretical models summarized in the appendix. SEY curves were fitted using a four-parameter semi-empirical model [1, 15]. BSEY curves were fitted using a three-parameter empirical model [1, 15]. Electron emission spectra were fit as the sum of a Chung-Everhart model for the emitted SE energy distributions and a Gaussian function for the BSE energy distribution [15, 35].

These theoretical models are important tools for estimating spacecraft outgoing currents and therefore potentials under varying space plasma conditions. Often spacecraft charging is simulated using standard charging codes such as NASCAP2K or SPIS [21, 22]. In this study, the ambient, SE, and BSE current densities were calculated using a standard model for electron emission from negatively biased surfaces [38].

Sections A-C in the appendix describe the parametric models used to fit the observed TEY, SEY, BSEY, and emitted electron energy distributions. These parametric models provide significantly higher accuracy representations of the SEY and BSEY [1] for current flux calculations than those using standard NASCAP fit parameters for SEY and BSEY [21] which are listed in Sec. H of the appendix for comparison. Sec. D, E and F in the appendix show the electron, SE and BSE current density calculation equations for different mission plasma environments. Sec. G in the appendix shows the equation used to plot normalized current density versus ambient electron temperatures.

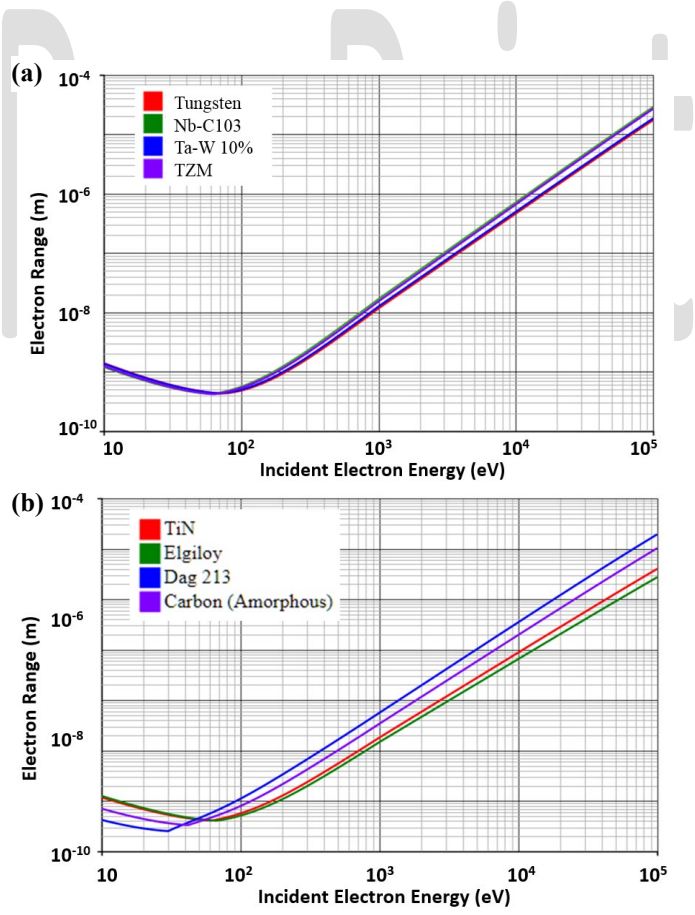

Fig. 3 Electron range versus incident energy. (a) W, Nb-C103, Ta-W 10% and TZM. (b) TiN, Elgiloy, Dag 213 graphite epoxy composite, and amorphous C as reference. Range calculated using refs. [2, 3].

TABLE III
BSEY FIT PARAMETERS

Sample	$E_{SE\,max}$ (eV)	$\left[\frac{E^a_{peak}-E^u_{peak}}{E^u_{peak}}\right]$*	η_{max}	$\left[\frac{\eta^a_{max}-\eta^u_{max}}{\eta^u_{max}}\right]$*	η_0	$\left[\frac{\eta^a_o-\eta^u_o}{\eta^u_o}\right]$*
W Un.	4000±4000		0.23±0.3		0.229±0.018	
W 1200°C	3000±2000	-25%%	0.29±0.02	***+29%***	0.273±0.016	***+19%***
Nb-C103 Un.	4200±1900		0.221±0.014		0.2297±0.0086	
Nb-C103 1200°C	20000±30000	+380%	0.26±0.03	+18%	0.23±0.10	+0.1%
TiN Un.	290±90		0.157±0.010		0.132±0.011	
TiN 180°C	800±400	***+176%***	0.171±0.011	+9%	0.14±0.017	+6%
Ta-W 10% Un.	3000±4000		0.31±0.03		0.27±0.10	
Ta-W 1200°C	2500±1600	-17%	0.30±0.12	-3%	0.27±0.04	0%
Molly TZM Un.	3000±3000		0.210±0.017		0.19±0.04	
Molly TZM 1200°C	4000±4000	+33%	0.24±02	+14%	0.19±0.18	0%
Elgiloy Un.	2000±1300		0.206±0.015		0.177±0.017	
Elgiloy 800°C	1400±1100	-30%	0.186±0.019	-10%	0.17±0.014	-4%
DAG-213 180°C	520±140		0.145±0.011		0.067±0.018	

* Values greater than uncertainties in italics

IV. Results

The following sections describe the TE, SE and BSE yields from the samples tested, including the TE, SE and BSE energy distributions and currents calculated for different ambient plasma parameters.

A. Secondary and Backscatter Electron Yield

The results of the TEY, SEY, and BSEY are shown in Figs. 4-10. Note these are log-log plots used to emphasize the effects of the power law fitting parameters *n* and *m* at lower and higher energies, respectively. DAG 213, shown in Fig. 4, did not have a unannealed sample tested. Tungsten, Nb-C103, TZM, Ta-W, Elgiloy, and TiN are shown in Figs. 5-10, respectively. In each of these figures, the yield of the unannealed sample is shown in plot (a) and that of the annealed sample in plot (b). Residual plots (c) show the percent change in yield due to annealing, for example $[(\sigma_{annealed} - \sigma_{unannealed})/\sigma_{unannealed}]$.

It is important to note that at low energies (10eV-50eV) errors can be rather large, estimated to be up to ±20% of the plotted yields at energies <30eV. A major source of errors in lower energy SEY and BSEY is the use of the conventional engineering definition employed in charging codes that categorizes electrons emitted with energies >50eV as BSE and those with energies <50eV as SE; obviously this definition fails to have any meaning for electron with incident energies <50eV.

These low energy errors can also be due to electron dynamics, as primary and SE are affected by stray and non-uniform electric and magnetic fields inside the chamber. The chamber is fitted with a two layer sleeve of μ-metal magnetic shielding to reduce ambient magnetic field inside the chamber by a factor of ≳10 [39], but other magnetic fields from the instrumentation could still induce errors. These disturbances to the electron trajectories lead to two major sources of errors: the number of electrons from the electron gun missing the target, and the number of electrons not captured by the grid [40]. In other words, not all electrons leaving the gun impact the sample, and not all the SE and BSE leaving the sample hit the grid, especially at low energies. Use of a (nearly) fully enclosed hemispherical detector captures and measures nearly all emitted electrons, except ~1-2% that can escape via a drift tube that allows incident electrons to reach the sample [39], thereby allowing this detection scheme to make high accuracy yield measurements, on the order of 2-3% for conductors and ~5% for insulators [33, 36]

Table II summarizes the SE yield fit parameters for all samples, based on the four-parameter semi-empirical equation (A1). These include δ_{max}, the maximum SE yield, E_{SEmax}, the incident electron energy where δ_{max} occurs, and two power law coefficients *n* and *m* related to the low energy and high energy slopes of log-log plots of SEY such as Fig. 4. The crossover energies, E_1 and E_2, defined as where the SE yield equals unity are also listed, as is the normalization constant r_{max}. These yield features are identified in Fig. 4. Similarly, Table III summarize the BSE yield fit parameters for all samples, based on the three-parameter empirical equation (A3).

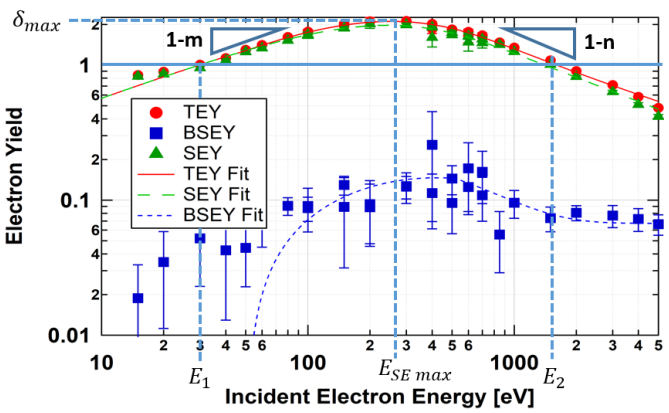

Fig. 4 DAG 213 TEY, SEY, and BSEY data and model fits for an annealed sample, between 10eV and 5keV incident electron energy. SEY fits are modeled with Eq. (A1) with fitting parameters listed in Table II. BSEY fits are modeled with Eq. (A2) with fitting parameters listed in Table III. Yield features, δ_{max}, E_{SEmax}, *n*, *m*, E_1, and E_2 are indicated on the plot.

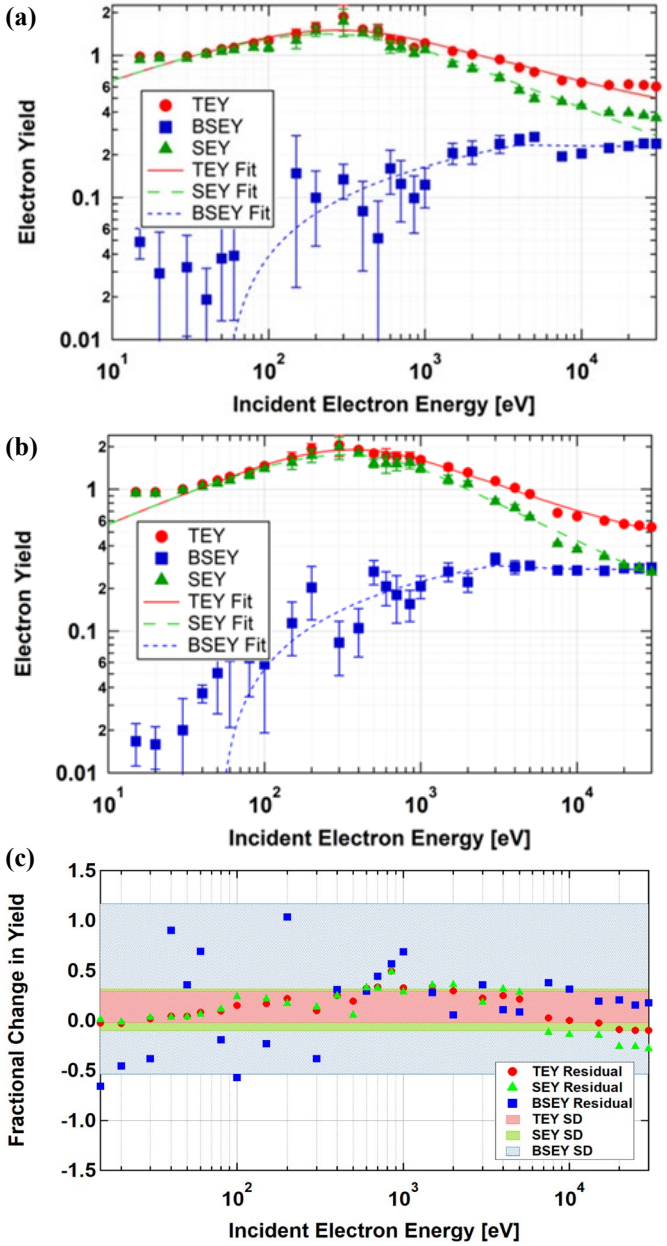

Fig. 5 Tungsten SE, BSE and TSE yields and model fits for incident electron energies between 10eV and 30keV. SEY fits are modeled with Eq. (A1) with fitting parameters listed in Table II. BSEY fits are modeled with Eq. (A2) with fitting parameters listed in Table III. (a) Unannealed sample. (b) Annealed sample. (c) Percent difference between annealed and unannealed samples, $\left[\frac{\sigma^a_{max}-\sigma^u_{max}}{\sigma^u_{max}}\right]$, *etc.*

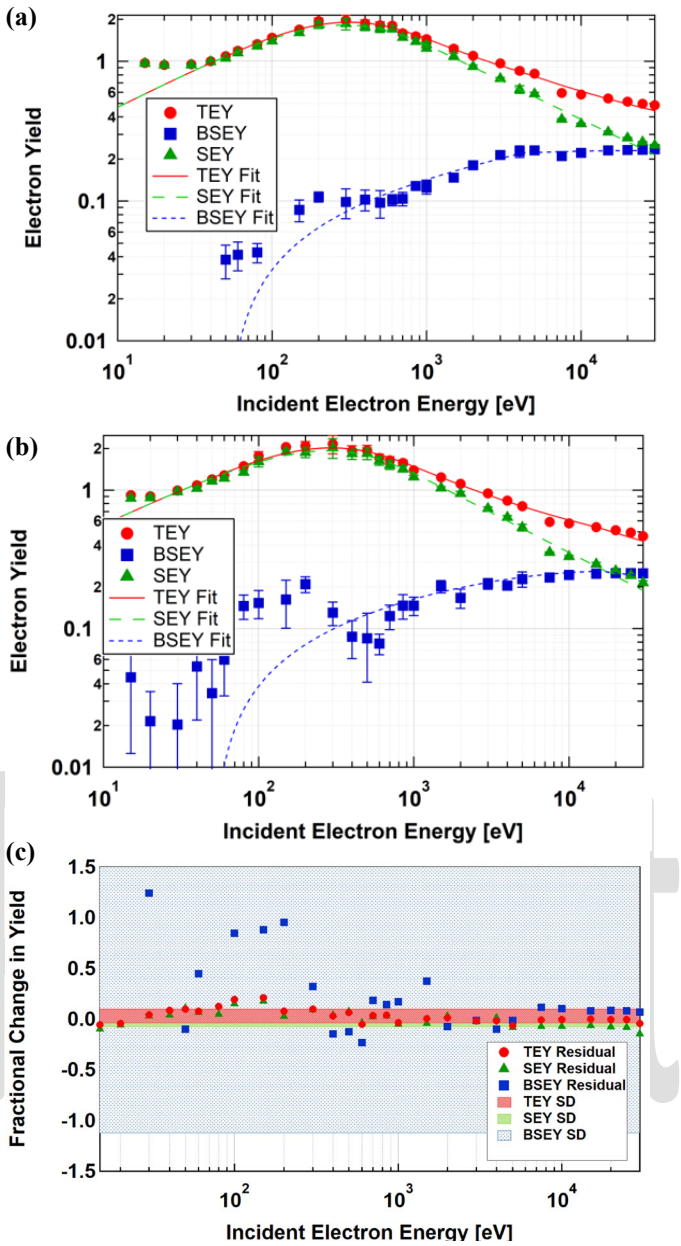

Fig. 6 Nb-C103 SE, BSE and TSE yields and model fits for incident electron energies between 10eV and 5keV. SEY fits are modeled with Eq. (A1) with fitting parameters listed in Table II. BSEY fits are modeled with Eq. (A2) with fitting parameters listed in Table III. (a) Unannealed sample. (b) Annealed sample. (c) Percent difference between annealed and unannealed samples, $\left[\frac{\sigma^a_{max}-\sigma^u_{max}}{\sigma^u_{max}}\right]$, *etc.*

The maximum sample SE yield, δ_{max}, changes between unannealed versus annealed samples of the materials, as noted in Table II. The maximum yield increased for Elgiloy, Molly TZM, Nb-C103, and Tungsten, with annealing of the sample, while it decreased or remained within the error of the unannealed sample for Ta-W and TiN. The residual curves of Fig. 5-10(c) demonstrate how both the TSEY, SEY and the BSEY have changed due to annealing. Shaded regions in Figs. 5-10(c) are bounded by the mean residuals for each yield ±1 standard deviation of the residuals.. Together, these provide a useful way to highlight energies at which statistically significant changes occur due to annealing. As expected, the relative changes are largest for BSE data (blue) where yields are small.

In addition, Table II shows differences in E_1 and E_2 for annealed versus unannealed samples. E_1 increases with annealing on Ta-W and Elgiloy, while it decreases on W, Nb-C103, and remains the same for TiN. E_2 increases for all samples except for Nb-C103, which decreases.

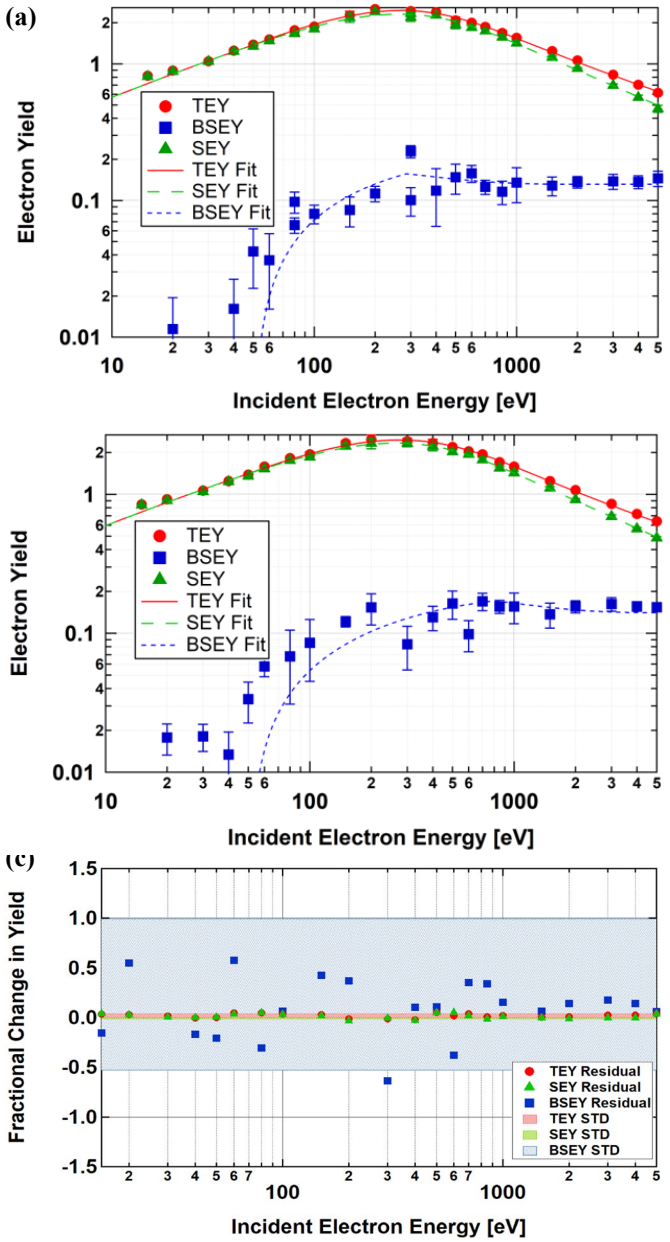

Fig. 7 TiN SE, BSE and TSE yields and model fits for incident electron energies between 10eV and 5keV. SEY fits are modeled with Eq. (A1) with fitting parameters listed in Table II. BSEY fits are modeled with Eq. (A2) with fitting parameters listed in Table III. (a) Unannealed sample. (b) Annealed sample. (c) Percent difference between annealed and unannealed samples, $\left[\frac{\sigma^{a}_{\max}-\sigma^{u}_{max}}{\sigma^{u}_{\max}}\right]$, *etc.*

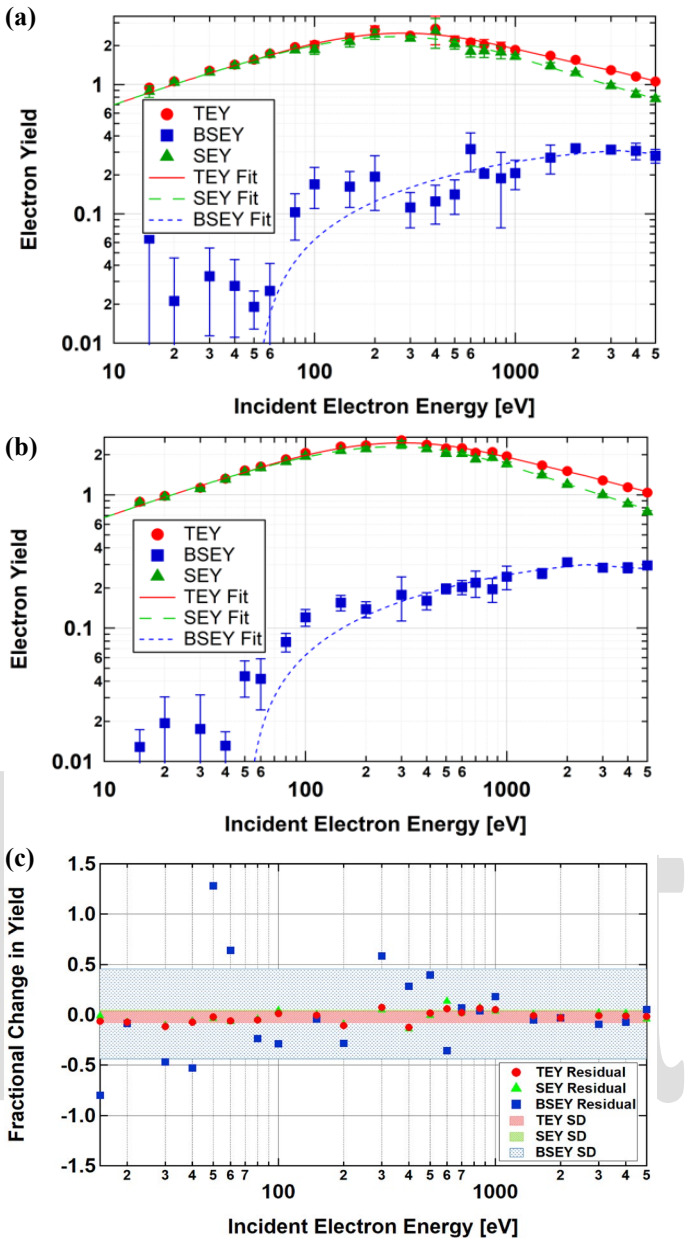

Fig. 8 Ta-W SE, BSE and TSE yields and model fits for incident electron energies between 10eV and 5keV. SEY fits are modeled with Eq. (A1) with fitting parameters listed in Table II. BSEY fits are modeled with Eq. (A2) with fitting parameters listed in Table III. (a) Unannealed sample. (b) Annealed sample. (c) Percent difference between annealed and unannealed samples, $\left[\frac{\sigma^{a}_{\max}-\sigma^{u}_{max}}{\sigma^{u}_{\max}}\right]$, *etc.*

All these differences will influence the material behavior in different ambient plasma, by changing the current induced by SEY and BSEY, as shown in Section C. The effects of relative changes of the SE and BSE fitting parameters on threshold charging have been quantified; it was found for the specific cases studied there that changes in $\delta_{\max}$ followed by changes in E_{SEmax}, had the largest effects on charging for several different representative space plasma environments [15].

Yield data for the composite material Dag 213 is shown in Fig. 4. As is expected [41] the yields are more similar to bisphenol epoxy yields, which constitute the vast majority of the composite material, than the yields of graphitic carbon, which have a low maximum yield typically just above unity at low E_{max}, near 200 eV [36]. Note that the probe beam does not cause the sample to exhibit signs of charging due to the ~10% conductivity microcrystalline graphite content that enhances conductivity in the sample and dissipates the charge from the probe beam.

Fig. 5 shows the results for W, where annealing has the effect of increasing the peak of the SEY curve (maximum yield) by

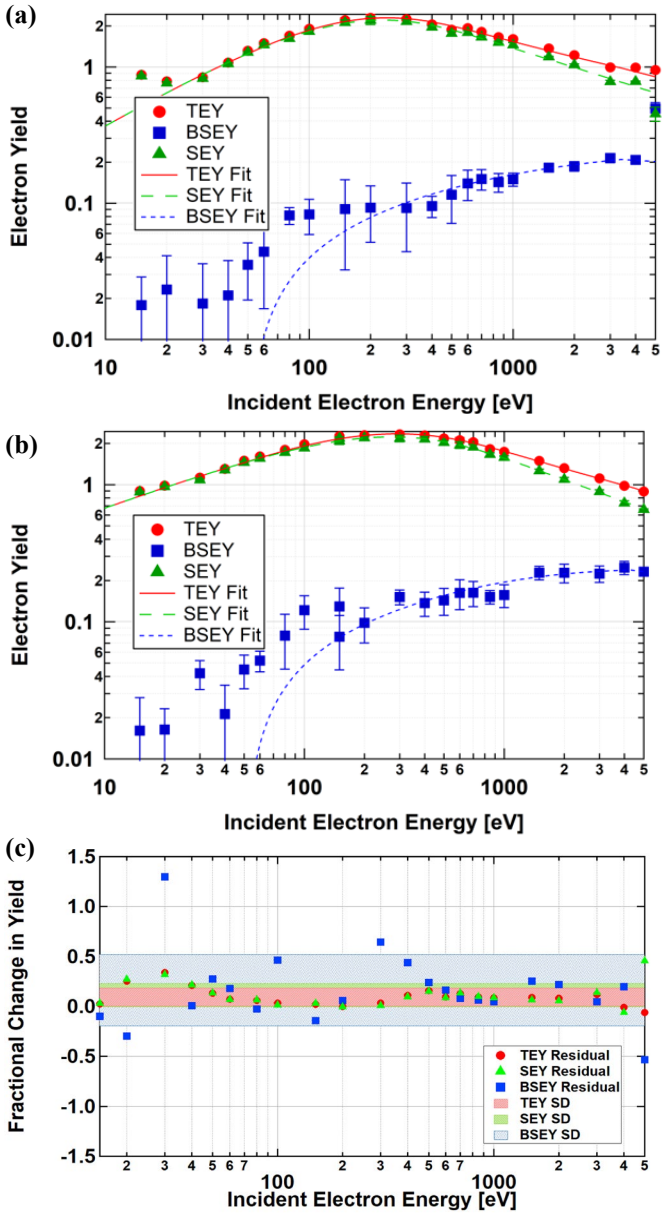

Fig. 9 TZM SE, BSE and TSE yields and model fits for incident electron energies between 10eV and 5keV. SEY fits are modeled with Eq. (A1) with fitting parameters listed in Table II. BSEY fits are modeled with Eq. (A2) with fitting parameters listed in Table III. (a) Unannealed sample. (b) Annealed sample. (c) Percent difference between annealed and unannealed samples, $\left[\frac{\sigma^a_{max}-\sigma^u_{max}}{\sigma^u_{max}}\right]$, *etc.*

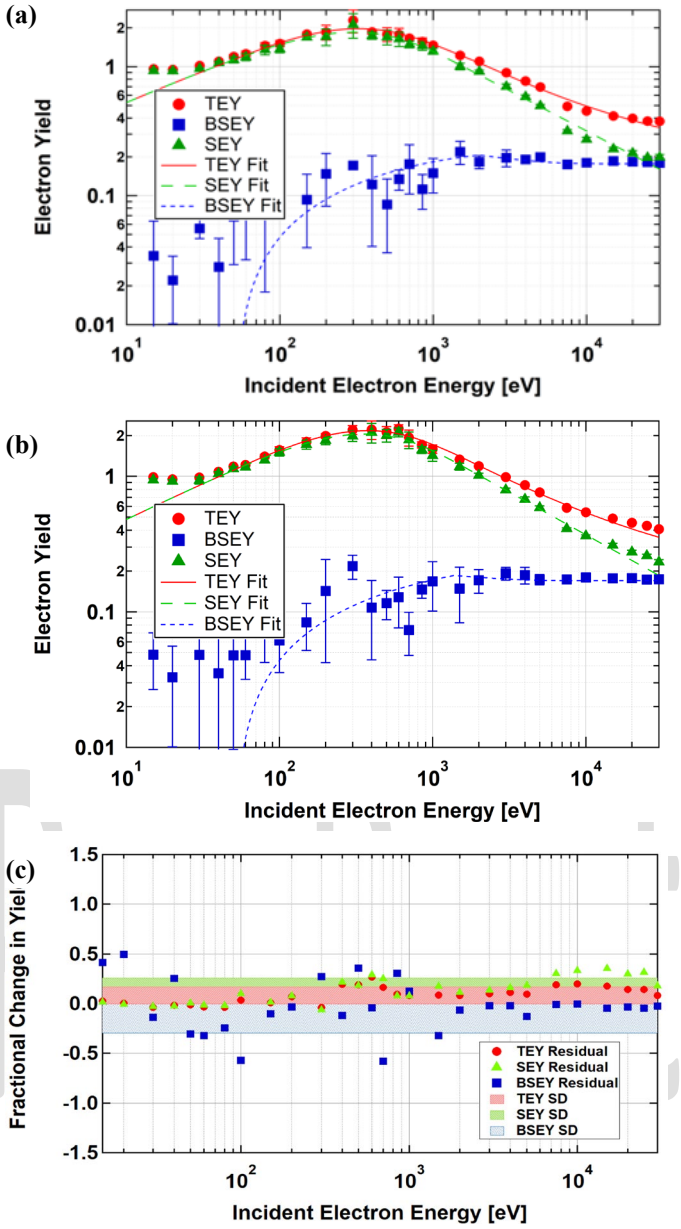

Fig. 10 Elgiloy SE, BSE and TSE yields and model fits for incident electron energies between 10eV and 30keV. SEY fits are modeled with Eq. (A1) with fitting parameters listed in Table II. BSEY fits are modeled with Eq. (A2) with fitting parameters listed in Table III. (a) Unannealed sample. (b) Annealed sample. (c) Percent difference between annealed and unannealed samples, $\left[\frac{\sigma^a_{max}-\sigma^u_{max}}{\sigma^u_{max}}\right]$, *etc.*

~13% and increasing the slopes at the lower (~13%) and higher energies (~180%). The maximum BSEY decreased ~25% due to annealing at higher energies. Annealing of the sample also has the effect of decreasing the incident energy where BSEY is greater than the SEY. This effect is also observed in other samples, including Nb-C103 and Elgiloy shown in fig. 6 and fig. 10.

Fig. 6 shows Nb-C103, with a modest ~11% increase in the maximum SEY yield and a ~11% decrease in E_{SEmax}, while the slope at lower energies remain constant and increases at higher energies. BSEY also increased due to annealing.

Note, there is evidence for two peaks in the unannealed Nb-C103 BSEY curve, one near 150 eV and one at much higher energies. The presence of two BSE peaks is even more evident in the annealed curve Fig. 6(b). A possible explanation for this has been proposed by Wilson for similar studies of a series of thin graphitic carbon layers with increasing thickness deposited

TABLE IV
FITS FOR ELECTRON EMISSION DISTRIBUTION

	Chung-Everhart SE fit				Gaussian BSE fit					
Sample	ϕ (eV)	$k_B T_E$ (eV)	$\left[\frac{T_E^a - T_E^u}{T_E^u}\right]$ *	$\frac{\eta(E_0)}{\delta(E_0)}$	f_{BSE}	$\left[\frac{f_{BSE}^a - f_{BSE}^u}{f_{BSE}^u}\right]$ *	E_0 (eV)	ΔE_E (eV) *	γ_0 $(eV)^{-1}$
W Unannealed	4.79±0.09	1.63±0.02		3.5%	4.8%±0.7%		53.63±0.18	2.6±0.3	0.0004 ± 0.0006
W (1200°C)	4.54±0.13	1.50±0.03	***-8%***	2.9%	5.8%±0.7%	***+21%***	53.48±0.13	2.8±0.3	0.0008 ± 0.0005
Nb-C1O3 Un.	4.68±0.16	1.56±0.06		3.5%	6.5%±0.8%		53.47±0.15	2.9±0.3	0.0005 ± 0.0007
Nb-C1O3 (1200°C)	4.74±0.07	1.61±0.02	+3%	2.9%	6.6%±0.7%	+2%	53.96±0.13	2.3±0.2	0.0008 ± 0.0006
TiN Un.	4.55±0.4	1.57±0.4		3.1%	10%±2%		53.75±0.14	2.9±0.6	-0.0012 ± 0.0006
TiN (180°C)	4.51±0.07	1.60±0.02	+2%	2.4%	6.1%±1.1%	***-41%***	53.7±0.2	2.8±0.4	-0.0002 ± 0.0009
Ta-W 10% Un.	4.74±0.10	1.59±0.02		1.2%	8.3%±1.1%		53.74±0.12	2.8±0.3	-0.0010 ± 0.0009
Ta-W (1200°C)	4.73±0.09	1.57±0.02	-1%	2.2%	5.9%±0.7%	***-30%***	53.77±0.11	2.45±0.19	0.0014 ± 0.0004
TZM Un.	4.67±0.10	1.59±0.03		2.7%	6.4%±0.6%		53.63±0.10	2.47±0.18	0.0004 ± 0.0005
TZM (1200°C)	4.71±0.09	1.61±0.02	+1%	3.0%	6.2%±0.6%	-3%	53.80±0.11	2.44±0.18	0.0013 ± 0.0004
Elgiloy Un.	4.49±0.19	1.47±0.07		5.7%	5.4%±0.9%		53.62±0.19	2.4±0.3	0.0018 ± 0.0006
Elgiloy (800°C)	4.68±0.11	1.57±0.03	***+7%***	4.0%	6.0%±0.7%	***+11%***	53.37±0.13	2.7±0.2	0.0009 ± 0.0005
DAG 213 (180°C)	4.72±0.09	1.57±0.02		3.4%	5.9%±0.9%		53.83±0.15	2.4±0.3	0.0008 ± 0.0006
Mean Value							53.67 ± 0.04	2.59 ± 0.05	0.0005 ± 0.0002

* Values greater than uncertainties in italics

on Au substrates [42]; there, the lower energy BSE observed at ~170 eV can be clearly attributed to the C layers and a higher energy peak attributed to the Au substrate. The more pronounced double peak for annealed Nb-C103 is consistent with the observation (see Table I) that this sample has approximately twice the carbon and oxygen contamination layers observed for other films. Similar, though less pronounced, double peaked BSEY curves are observed for Ta-W [Figs. 8(a-b)] and unannealed TZM [Fig. 9(a)], suggesting similar organic contamination layers for these samples.

Fig. 7 shows TiN, where the annealing effects on SEY were very small, compared to other samples tested. The annealing temperature of TiN was much lower than the other samples and might have affected the amount of cleaning and smoothing on the sample. The effects on BSEY were larger, increasing E_{max} for the annealed sample.

In fig. 8 there are two peaks in the SEY unannealed samples of Ta-W, probably due to contamination of the surface (as discussed above). The BSEY double peak structure for the Ta-W sample is significantly reduced after annealing. This double peak structure is even evident in the TEY curve. During annealing of the surface *in vacuo*, contamination is removed leading to a smooth single TEY peak, very similar in shape and form to the unannealed sample. Annealing cleaning and smoothing surface effects have been previously explored for W and Moly-TZM [37] with a scanning electron microscope (SEM). This double peak and removal of contamination is also observed in Ta-W and TZM, shown in Fig. 9.

The Elgiloy SEY and BSEY results are shown in Fig. 10. The annealing increased the maximum yield and the slopes have also increased at higher and lower incident energies. Annealing increased the BSEY.

B. *Electron Emission Energy Distributions*

The SE and BSE energy distributions were measured for all samples for ~53eV incident electron energy. As an example,

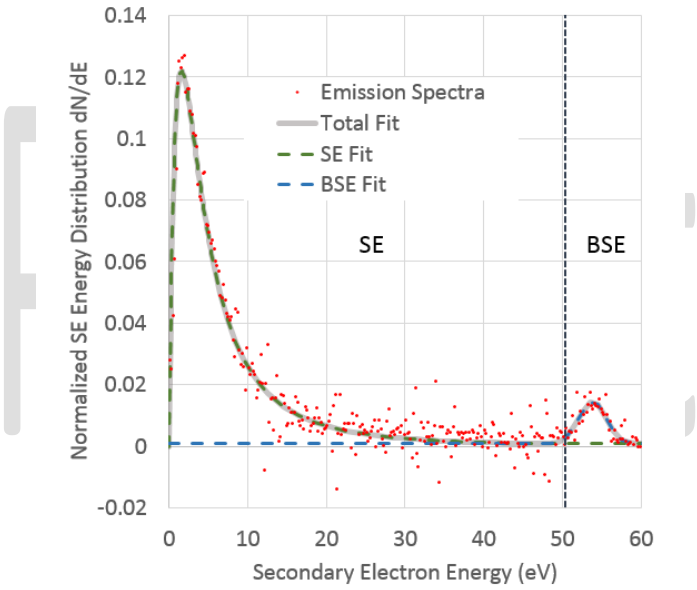

Fig. 11 DAG213 SE and BSE data and fit energy distribution, annealed sample.

Fig. 11 shows the normalized SE and BSE energy distribution (number of particles emitted per unit energy per incident electron, *dn/dE*) of DAG 213 along with the fitted Chung-Everhart (SE) and Gaussian (BSE) models. As expected, the BSE Gaussian fits have a very reproducible maximum of 53.67 ± 0.04 eV (see Table III), close to the incident electron energy of ~53eV and a BSE peak width of 2.59 ± 0.05 eV, in agreement with the instrumental resolution estimated in Sec. II.

The energy distribution in Fig. 11 has been normalized such that the area under the curve is equal to unity. Absolute yield distributions are obtained by multiplying the normalized distribution by the energy-dependent yield, $\delta(E_0)$. Recall, by convention, electrons with emission energies <50eV are considered SE, while everything at higher emission energies is considered BSE. Comparison of the parameter f_{BSE} to the ratio

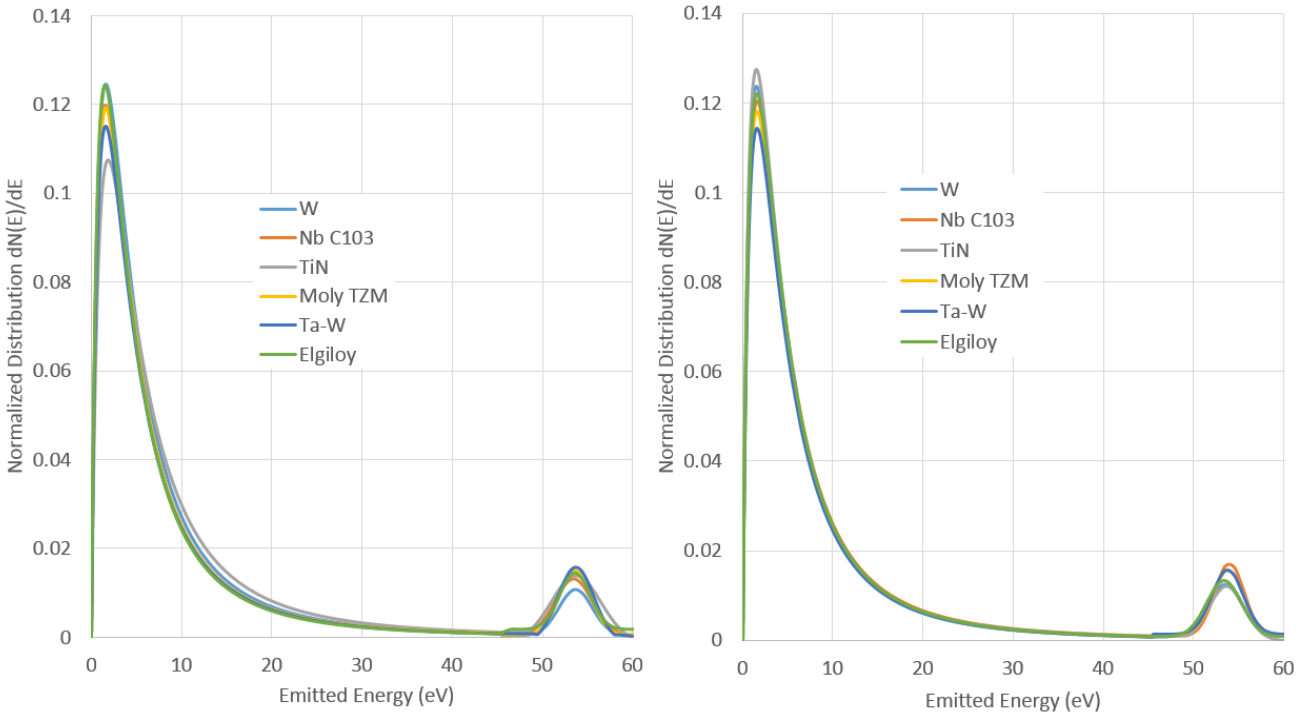

Fig. 12 SE and BSE energy distribution fits of W, Nb-C103, TiN, Moly-TZM, Ta-W and Elgiloy. (a) Results for unannealed samples. (b) Results for annealed samples.

$\eta(50eV)/\delta(50eV)$, provides a measure of the errors introduced in low energy yields from the operationally distinction SE and BSE at 50 eV employed in both measurements and yield fitting functions. Values for f_{BSE} are consistently higher than the ratio $\eta(50eV)/\delta(50eV)$, by about a factor of 2; this is consistent with the notion that about half of BSE electrons with a Gaussian distribution of width would be measured as BSE by a detector with finite resolution ΔE_E. At incident energies below 50 eV, the measured BSEY is typically in the range of 0.01 to 0.04, at or below the instrumental resolution of yields; this is related to the offset y_o for the BSEY energy distribution (see Table IV). No significant changes in f_{BSE} are observed as a result of annealing.

Figure 12 shows the normalized distribution *dn/dE* of W, Nb-C103, TiN, Moly-TZM, Ta-W and Elgiloy. Fig. 12(a) shows the results from the unannealed samples, and Fig. 12(b) those from the annealed samples. In each case, the peak at low energies (below 10 eV) is from the SE energy distribution and that near 53 eV is from the BSE energy distribution. The shapes of the curves are very similar, although the relative contributions from SE and BSE differ somewhat from material to material as characterized by the differences in the parameter f_{BSE} and the ratio $\eta(50eV)/\delta(50eV)$ listed in Table IV.

Table IV shows the parameters of the SE Chung-Everhart model fits. This table also shows the energy of the peak of the SE energy distribution (k_BT_{se}, in eV) of the SE distribution. The measured values of k_BT_{SE} were within the range of values measured for metals in prior experiments of 1.3 to 2.5eV[34]. Annealing had at most modest effects on T_{SE} of the samples. The energy of maximum number of SE did not change due to annealing (≤3%) by an amount larger than the uncertainties for most samples, the exceptions being that it increased for Elgiloy by ~7% and decreased for W by ~8%.

As shown by Chung-Everhart [35] k_BT_{SE} is directly proportional to the material's work function Φ, as $k_BT_{SE} = ⅓Φ$. Agreement between work functions estimated as a fitting parameter and from the peak position were in very good agreement, within 0.01 eV or less (except for annealed TiN). The estimated work function for annealed W—the effective calibration standard for this study— using this relation determined from energy spectra using this relation (see Table IV, column 2) was in excellent agreement with previous measurements and recommendations of 4.55eV [4, 43-45]. TiN, Nb C103, TZM, TaW and Elgiloy estimated work functions are ~0.38 eV or 9% larger than prior measurements and ~0.4 eV or ~10% larger than estimates found with a

TABLE V
AVERAGE ELECTRON PLASMA PARAMETERS AT MAGNETOSHEATH, GEO, AND SOLAR WIND

	Electron density (cm^{-3})	Electron temperature (eV)	Current Density ($\mu A/m^2$)
1 AU	6.93	8.14	1.06
0.75AU	13.51	10.41	2.34
0.25AU	116.12	22.95	3.28e2
9.5Rs	4022	84.87	1.98e3
GEO	0.78	550	1.26
	0.31	8680	
Magnetosheath	17	7.76	2.55

TABLE VI
UNANNEALED AND ANNEALED MATERIAL SE CURRENT DENSITIES (μA/m^2) WITHOUT REDUCTION DUE TO TEMPERATURE

Sample	1AU	0.72AU	0.25AU	9.5Rs	GEO	Magentosheath
Previous W measuements	0.60	1.51	28.7	2930	1.44	1.39
W Unannealed	0.74	1.77	28.5	2416	1.16	1.74
W (1200°C)	0.63	1.55	27.2	2661	1.39	1.48
Nb-C1O3 Unannealed	0.56	1.41	26.8	2887	1.55	1.31
Nb-C1O3 (1200°C)	0.60	1.51	28.4	2955	1.38	1.64
TiN Unannealed	0.68	1.72	33.2	3548	1.57	1.59
TiN (180°C)	0.70	1.77	34.1	3625	1.55	1.63
Ta-W 10% Unannealed	0.83	2.06	37.8	3711	1.72	1.93
Ta-W (1200°C)	0.78	1.93	35.2	3507	1.71	1.82
TZM Unannealed	0.54	1.47	35.1	5095	2.99	1.24
TZM (1200°C)	0.77	1.91	34.7	3423	1.60	1.80
Elgiloy Unannealed	0.61	1.51	27.6	2820	1.36	0.91
Elgiloy (800°C)	0.58	1.45	27.5	3031	1.60	1.35
DAG 213 (180°C)	0.66	1.65	30.5	3014	1.26	1.55

TABLE VII
UNANNEALED AND ANNEALED MATERIAL BSE CURRENT DENSITIES (μA/m^2)

Sample	1AU	0.72AU	0.25AU	9.5Rs	GEO	Magentosheath
W Unannealed	7.88E-06	6.82E-05	1.36E-02	6.07	1.12E-02	1.38E-05
W (1200°C)	1.58E-05	1.36E-04	2.72E-02	12.05	2.10E-02	2.78E-05
Nb-C1O3 Unannealed	9.77E-06	8.46E-05	1.69E-02	7.57	1.45E-02	1.72E-05
Nb-C1O3 (1200°C)	8.32E-06	7.21E-05	1.44E-02	6.42	1.20E-02	3.29E-05
TiN Unannealed	2.47E-05	2.13E-04	4.15E-02	16.21	1.46E-02	4.35E-05
TiN (180°C)	1.29E-05	1.12E-04	2.21E-02	9.30	1.13E-02	2.27E-05
Ta-W 10% Unannealed	1.99E-05	1.72E-04	3.44E-02	15.10	2.49E-02	3.48E-05
Ta-W (1200°C)	2.23E-05	1.93E-04	3.85E-02	16.93	2.80E-02	3.93E-05
TZM Unannealed	1.21E-05	1.05E-04	2.09E-02	9.23	1.56E-02	2.13E-05
TZM (1200°C)	1.76E-05	1.52E-04	3.03E-02	13.31	2.16E-02	3.09E-05
Elgiloy Unannealed	1.62E-05	1.40E-04	2.78E-02	12.15	1.88E-02	2.85E-05
Elgiloy (800°C)	1.32E-05	1.14E-04	2.28E-02	9.97	1.54E-02	2.33E-05
DAG 213 (180°C)	2.21E-05	1.90E-04	3.67E-02	13.70	9.26E-03	3.90E-05

Vergard-like approach from tabulated elemental work functions (see Table I, column8) [4]. DAG213's estimated work function was similar to past measurements [45], and approximately equal to the band gap energy for typical epoxy materials.

Annealing also varied the BSE energy spectra compared to the unannealed samples. The material-dependent fraction of BSE in the emission spectra, f_{BSE}, varied due to annealing. f_{BSE} increased for W and Elgiloy, while it decreased for Ta-W and TiN. Table IV shows the parameters of the BSE Gaussian model fit.

C. SE and BSE Current Densities

The current due to SE was calculated for all materials in different space environments, such as GEO experienced mostly by Van Allen Probes and the magnetosheath experienced by MMS in their high eccentricity orbits. The current was also calculated in the solar wind at 1AU, 0.72AU, 0.25AU experienced by Solar Orbiter and even closer to the Sun 9.5Rs by PSP. Table V shows the electron temperature and number density of these plasma environments. The GEO plasma environment is considered a two-electron population plasma [38]. The current calculations for the magnetosheath use average electron temperatures at 7.8eV which is in the same order of magnitude to the SEY population of 1-2 eV.

Other environments not included are the plasmasphere and the ionosphere with few eV of electron population. While the densities in each region are quite high, the temperatures are lower than the value of E_1 for these materials, leading to insignificant SE and BSE fluxes in those environments.

Fig. 13 shows on the left axis the ambient differential electron number flux versus electron energy in these different plasma environments. The SEY of the annealed and unannealed W sample is shown on the right axis of Fig. 13.

The annealed W SE yield curve is not consistently larger or smaller than the unannealed one, making the W annealed and unannealed SE current densities behave differently (larger/smaller) depending on the incident electron environment. In contrast, the BSE yield curve (at least above 100 eV) is consistently larger for annealed W (not so for the

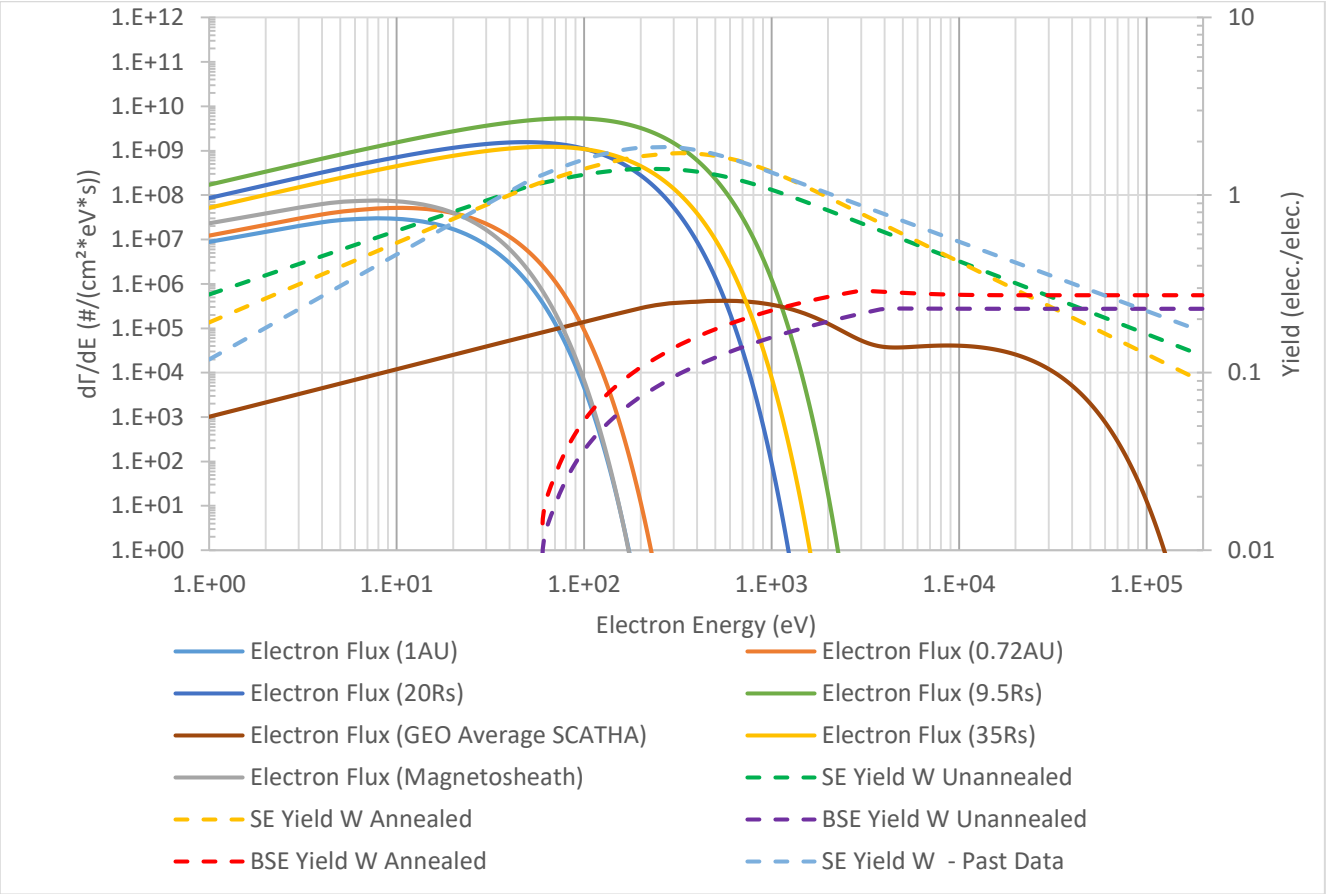

Fig. 13 Differential Electron Number Flux in different plasma environments and the SE and BSE yield of W annealed and unannealed. Flux left axis, yield right axis. Past tested W fit was added to compare with current W fits.

other samples), which makes the BSE currents always larger for the annealed sample in all environments.

A W SEY curve fit from past experiments [1] was also added to compare with the new fits. The new tested unannealed W yield fits are comparable with past data, but not equal, with a SEY peak at similar incident electron energy, but smaller than the previously tested W. The slope on the right side of the peak of the previously tested W is similar to that of the unannealed sample, and steeper on the low energy side of the peak.

These variations are probably due to different surface treatment prior to testing. Similar studies of W available in the literature [46-50] show a wide variance in measured yield curves; such large differences are common in the literature as even modest variations on surface contamination, surface morphology, instrumentation calibration for absolute yields are often not well documented or taken into account [51]. This makes comparison of absolute yields from different studies challenging [36].

The annealed sample showed clear differences in maximum peak, and slopes before and after the peak, as seen in Fig. 12. The maximum yield occurred at a greater electron energy for the annealed sample. Current densities of the past measured data are lower at electron energies below the peak for both annealed and unannealed W.

The current density of past measured W has larger current densities above the peak. Table VI shows the SE current densities calculated for the unannealed and annealed samples, at electron plasma environments described in Table V; fit results for a previous study of a clean technical W sample at USU are also listed. Annealed W current densities were within 10% of current densities for these previous tests, while unannealed W was within 25% of the previous observed current densities. This suggests that annealing had a significant effect of the W yields, perhaps by driving off contamination.

For PSP, not only does the electron flux and temperature change at different distances from the Sun, but the temperature of the sample increases significantly as the SC approaches perihelion. Temperatures of the FIELDS antennas will reach more than 1400K.

The SE current densities shown in Table VI are estimates for the samples at ambient temperature. Past tests by Sternglass [52], McDonnell [53] showed how metal samples of platinum, tantalum and carbon, decreased their SEY by 0.07, 0.06 and 0.05 % per Kelvin, in contrast with the BSE which hardly changed.

Estimates of Nb, Mo, Ta and W [54] indicate an estimated reduction of 37%, 27%, 31% and 33% of the SE yield at elevated temperatures close to 1400K. More recent investigations [55] indicate a reduction of 31% for TiN for

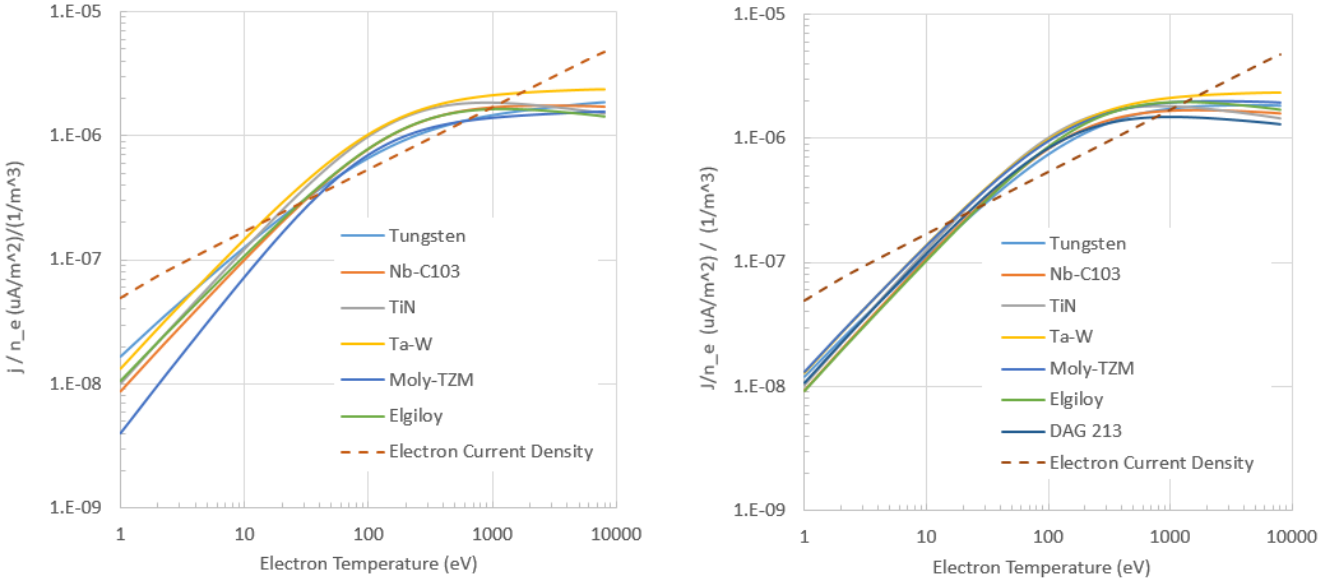

Fig. 14 Primary electron, and SE current densities per electron number density for W, Nb-C103, TiN, Ta-W, TZM, Elgiloy, and DAG 213. (a) Results for unannealed samples. (b) Results for annealed samples. The dashed line indicates the electron current density.

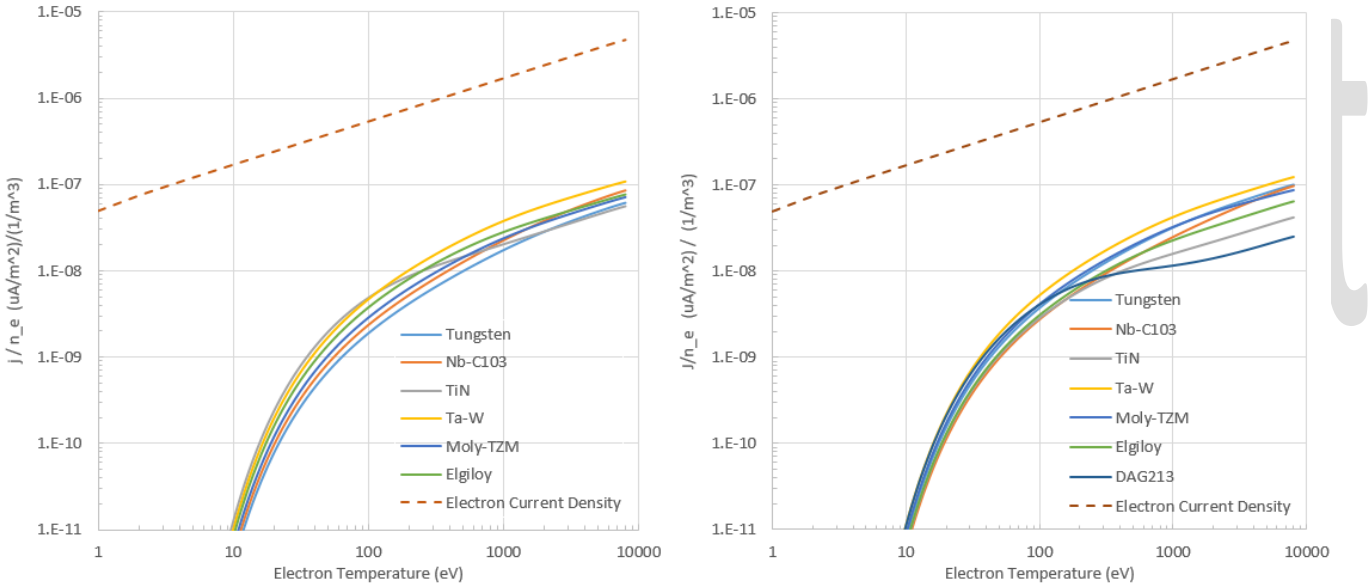

Fig. 15 Primary electron, and BSE current densities per electron number density for W, Nb-C103, TiN, Ta-W, TZM, Elgiloy, and DAG 213. (a) Results for unannealed samples. (b) Results for annealed samples. The dashed line indicates the electron current density.

temperature close to 673K. Taken together, these eight studies of high temperature conducting materials all have a negative temperature coefficient of change for SEY, with a reasonably consistent value of 0.05%±0.03% per Kelvin.

Even though some of the materials tested are different from these past data, except W and TiN, these trends of decreased SEY at hot temperatures would reduce the influence of SE induced currents. As SC approach the Sun, the solar photon flux increases, increasing the photocurrent, and increasing the surface temperature. This increase in temperature decreases the SE current densities. Table VI does not show this reduction of current density due to temperature, but it does show the annealing effects on current densities at different environments.

Unannealed W has larger SE current densities at 1AU, 0.75AU, 0.25AU and Magnetosheath than annealed W. Unannealed Nb-C103 has larger SE current densities for all plasma environments compared to annealed sample. Annealed TiN has larger SE current densities for GEO and the Magentosheath, and the SE current densities are the same for 1AU, 0.72AU, 0.25AU and 9.5Rs. Even though designers will not use TiN or DAG 213 for instruments exposed to the Sun as close as 9.5Rs, PSP has many instruments protected by the

Sunshield during close encounters with the Sun which maintain temperatures below 150°C, which are exposed to the plasma environment but not the solar photon flux.

Annealed Ta-W has larger SE currents for all plasma environments compared to unannealed. Annealed TZM has larger SE current densities at 1AU, 0.72AU and Magnetosheath, similar SE currents at 0.25AU, and smaller SE currents at 9.5Rs and GEO. Annealed Elgiloy has higher SE current densities for all plasma environments except for GEO, which is equal to the unannealed Elgiloy.

Table VIII show the BSE current densities of the unannealed and annealed W, Nb-C103, TiN, Ta-W, TZM, and Elgiloy. DAG 213 current densities are shown only for annealed. At 1AU, 0.72AU and Magnetosheath the BSE current densities are at least two orders of magnitude smaller than the SE current densities, and changes in BSE currents due to annealing effects would not affect the current balance.

Annealed W has larger BSE current densities for 0.25AU, 9.5Rs, and GEO than unannealed W. Unannealed Nb-C103 has larger BSE current densities for 0.25AU, 9.5Rs, but smaller for GEO than annealed Nb-C103. Annealed TiN has larger BSE current densities for 0.25A, 9.5Rs and GEO than unannealed TiN.

Unannealed Ta-W has smaller BSE current densities for 0.25AU, 9.5Rs, but larger for GEO than annealed Ta-W. Annealed TZM has larger BSE current densities for 0.25AU 9.5Rs and GEO than unannealed TZM. Unannealed Elgiloy has larger BSE current densities for 0.25AU, 9.5Rs, but smaller for GEO than annealed Elgiloy.

D. Current Densities per Electron Number Density

The electron current densities per number density were calculated for single Maxwellian plasma from 1eV to 8keV ambient plasma electron temperatures. The SE and BSE current densities per number density were also calculated from 1eV to 8keV ambient plasma electron temperatures. The SE and BSE electron current densities per number densities are plotted in Fig, 14 and Fig. 15 respectively. Fig.14 shows how the materials between ~20eV and ~2keV have a larger SE current than primary electron current. The annealing effects can be seen in the currents, both in the total current density per number density as well as the points where the SE currents are greater than the primary currents

Fig. 15 shows how the BSE current densities per number densities are very small at temperatures lower than 30eV, compared to the primary current densities per number densities. As the electron temperature increases to 8keV, the BSE current densities per number densities are in the same order of magnitude than the SE current densities per number densities.

For a quick estimate of the current balance calculation of a surface in space (in the shade), an engineer or scientist may assume a temperature and from the plots estimate the primary electron current, the SE current and the BSE current. Note that the primary electron currents will have an opposite sign to the SE and BSE currents in the current balance equation.

V. CONCLUSION

TE, SE, BSE and yields were measured and fitted for different sample materials for seven materials of particular relevance to spacecraft in high-temperature, high flux environments. The SE and BSE normalized energy distribution were also measured and fitted. The initial samples tested were unannealed and in conditions typical for spacecraft materials at launch; subsequent tests were conducted after annealing to high temperatures representative of the Parker Solar Probe mission, which might be expected to drive off contamination and even smooth rougher surfaces through thermal annealing. Small, but potentially significant, changes in the materials electron emission properties were observed. The results show how the SEY and BSEY characteristics of the materials can evolve through exposure to extreme environments typical of these new close-to-the-Sun missions, as observed in the SE and BSE current density calculations. The SEY and BSEY were used to calculate current densities in different plasma environments, showing how the annealing effects of the materials varied depending on the environment. The current densities per number densities were also plotted for primary electrons, SE, and BSE to aid in the design of instruments and spacecraft.

Based on these results, we conclude that it is vital for SC designers to incorporate both induced changes of materials properties and materials induced changes to the plasma environment in their SC charging calculations as they can affect equilibrium potentials [31, 56]. Engineers and scientists who use codes such as NASCAP or SPIS for SC charging assessments could benefit from use of the material data presented in this paper.

APPENDIX

The following sections (Sec. A-C) describe the parametric models used to fit the observed SEY, BSEY, and emitted electron energy distribution. Sec. D, E and F show the electron, SE and BSE current density calculation equations for different mission plasma environments. Sec. G shows the equation used to plot normalized current density versus ambient electron temperatures. Section H shows the NASCAP fit parameters.

Electron yield is an incident energy-dependent measure of the interactions of incident electrons with a material and characterizes the number of electrons emitted per incident electron. The total electron yield (TEY), $\sigma(E_0)$, is defined as the ratio total emitted electron flux to the incident flux,

$$\sigma(E_0) \equiv N_{out}^{e-}/N_{in}^{e-} = \delta(E_0) + \eta(E_0) \quad (A1)$$

It is separated into two terms, the secondary electron yield (SEY), $\delta(E_0)$, and backscattered electron yield (BSEY), $\eta(E_0)$.

A. Secondary Electron Yield Models

SEY describes electrons emitted from the material which originate within the material and are excited through inelastic collisions with the incident electrons; operationally SE are defined as electrons with emission energies <50 eV. Experimentally, SEY is determined by subtracting the BSEY from the TEY.

There were several different fits studied for each material, including Sternglass[52], Dionne[57] and Hastings[38] fits, as reviewed by Lundgreen[58].

All of the sample SE yields shown in Figs. 3-10 were fit using a four-parameter semi-empirical equation in reduced format derived from a 1D scattering model for the SE in the material [32]:

$$\delta(E_0) = \frac{\delta_{max}}{[1-e^{-r_{max}}]} \cdot \left(\frac{E_0}{E_{max}}\right)^{1-n} \cdot \left[1 - e^{\left(-r_{max}\cdot\left(\frac{E_0}{E_{max}}\right)^{n-m}\right)}\right] \quad \text{(A2)}$$

where E is the primary electron incident energy. Fitting parameters include δ_{max}, E_{max}, and two power law coefficients n and m related to the low energy and high energy slopes of log-log plots of SEY such as Fig. 4. r_{max} is a parameter dependent on n and m and fully determined by normalization of the fitting function. Details of the fitting function and parameters are given in [58]. This model is functionally similar to a model by Sims used with the SPIS code [59].

B. Backscatter Secondary Electron Yield Models

BSEY describes electrons emitted from the material which originate from the incident beam; operationally BSE are defined as electrons with emission energies >50 eV. Many BSE interact with the material largely through elastic (or nearly-elastic) collisions and are emitted with energies near the incident energy, E_0. Other BSE undergo one or more quasi-elastic collisions, but still escape with energies higher than most SE.

An extended three-parameter empirical model has been developed to model BSEY[32, 58]:

$$\eta(E) = \begin{Bmatrix} 0 & if\ E \le 50eV \\ \frac{log\left(\frac{E}{50eV}\right)}{log\left(\frac{E_{max}}{50eV}\right)}\,\zeta(E) & if\ 50eV < E < E_{max} \\ \zeta(E) & if\ E \ge E_{max} \end{Bmatrix} \quad \text{(A3)}$$

where ζ is defined as

$$\zeta(E;\eta_{max},\eta_0,E_{\text{peak}}) = e\left(\eta_{max}-\eta_0\right)e^{-(E/E_{\text{peak}})} + \eta_0 \quad \text{(A4)}$$

E_{peak} is the energy where the BSE yield peaks, η_{max} is the yield value at E_{peak}, and η_0 is the high energy asymptotic value at energies $\gg E_{peak}$. This has the same functional form as an empirical model proposed by Prokopenko and LaFroamboise'[60]. The single-parameter NASCAP fit to BSEY sets E_{peak}=5 keV and $e\left(\eta_{max}-\eta_0\right) = 0.1$, with η_0 specified through the fitting parameter Z_{eff} for an effective atomic number [21]. A similar relation for the SPIS BSEY fit differs slightly from NASCAP fit only above 10 keV [22]. As a first approximation, Z_{eff} can be set to the mean atomic number averaged over the stoichiometry for non-elemental materials, $\bar{Z}$ (see Table AII) [21, 22]

C. Emitted Electron Energy Distribution Model

The normalized TE emission spectrum is the weighted sum of the normalized SE and BSE spectra

$$\frac{dn_{TE}(E)}{dE} = (1 - f_{BSE}) \cdot g_{se}(E) + f_{BSE} \cdot g_{Bse}(E) + y_0 \quad \text{(A5)}$$

where f_{BSE} is the fraction of emitted electrons that are BSE. y_0 is a small offset to correct for instrumental effects and equal to the BSEY at E=0. Emission spectra typically have two main peaks corresponding to SE and BSE, modeled by the normalized distribution functions $g_{se}(E)$ and $g_{Bse}(E)$, respectively. Representative energy distributions of emitted electrons are shown in Figs. 11 and 12.

The shape of the distributions (A5) is very largely independent of the incident energy (or even what the source the incident energy is); incident energy only affects the emission spectra amplitudes through the energy-dependent yield, $\sigma(E_0) = \delta(E_0) + \eta(E_0)$. Multiplying the normalized distributions (A5), (A6) or (A7) by their corresponding yields gives the absolute electron emission spectra. Comparison of the parameter f_{BSE} to the ratio $\eta(50eV)/\sigma(50eV)$, provides a measure of the errors introduced in low energy yields from the operationally distinction SE and BSE at 50 eV.

The normalized SE distribution, $g_{se}(E)$, rises quickly from zero emitted energy to a peak energy at $E_{CE} = \frac{1}{3}\Phi$, usually between 1 eV and 3 eV; it then decays more gradually back to zero at higher energies. The Chung-Everhart model [35] describes this emitted SE energy distribution, which is[58]:

$$g_{se}(E) = \left\{\frac{6\cdot(E/\Phi)}{[1+(E/\Phi)]^4}\right\}. \quad \text{(A6)}$$

Φ is the vacuum energy surface barrier for emission, which is the work function for a conductor [33, 35] or the electron affinity for dielectrics and semiconductors[39, 61, 62]. For SE to escape a material, the electron must have enough energy to cross this vacuum barrier.

The BSE distribution has an upper cutoff above E_0, set by elastically scattered primary electrons, with a tail at lower energies for incident electrons that undergo one or more lower energy inelastic collisions. The measured BSE distribution is a convolution with an instrumental broadening function. This is typically modeled as a normalized Gaussian with width ΔE_E as[32, 58]:

$$g_{bse}(E) = \left\{[2\pi\cdot(\Delta E_E)^2]^{-1/2}\cdot exp\left[\frac{(E-E_0)}{\sqrt{2}(\Delta E_E)}\right]^2\right\} \quad \text{(A7)}$$

The approximation of the BSE distribution as such a Gaussian largely neglects contributions to the BSE distribution due to quasielastic scattered electrons, which are usually only on the order of 10% of BSE electrons.

D. Ambient Electron Current Density

The electron current density was calculated using [38]

$$j_e = -q_e\frac{2\pi}{m_e^2}\int_{E^*}^{\infty} EdE\int_0^{\pi} sin\theta d\theta\ \ f(E) \quad \text{(A8)}$$

where q_e is the electron charge, m_e is the electron rest mass, $f(E)$ is the energy distribution function of the incoming electrons with energy E, and Θ is the angle from surface normal of incident electrons. The lower bound of the distribution E^* is

$$E^* = \begin{vmatrix} 0 & V_s \le 0 \\ q_eV_s & V_s > 0 \end{vmatrix}$$

for a surface potential, V_s.

The energy distribution function can be defined as a single Maxwellian distribution:

$$f = n_e\left(\frac{m_e}{2\pi kT_e}\right)^{3/2} exp\left(-\frac{E}{k_BT_e}\right) \quad \text{(A9)}$$

where n_e is the electron number density of the plasma environment, T_e is the electron plasma temperature, and k_B is the Boltzmann constant.

E. SE Current Density

The SE current densities were calculated using the following equation [38]:

$$j_{SE} = -e\frac{2\pi}{m_e^2}\int_0^\infty dE_{se}\int_{E^*}^\infty EdE\int_0^\pi sin\theta d\theta\; g_{se}(E_{se},E)\;\delta_{1D}(E,\theta)\;f(E) \quad \text{(A10)}$$

where m_e is the electron mass, f(E) is the energy distribution function of the incoming electrons with energy E, $\delta_{1D}(E,\theta)$ is the SE yield as a function of E found in eq. 1, $g(E_{se}, E)$ is the normalized emission spectrum of SE with energy E_{se} due to incident electrons with energy E, and Θ is the angle from surface normal.

F. BSE Current Density

The BSE current densities were calculated using [13]:

$$j_{SE} = -q_e\frac{2\pi}{m_e^2}\int_0^\infty dE_{se}\int_{E^*}^\infty EdE\int_0^\pi sin\theta d\theta\;\delta(E,\theta)\;g_{se}(E_{se},E)\;f(E) \quad \text{(A11)}$$

where $\delta(E,\theta)$ is the SE yield as a function of E given by Eq. (A2), $g(E_{se}, E)$ is the normalized emission spectrum of SE with energy E_{se} due to incident electrons with energy E , and Θ is the angle from surface normal.

G. Current Density per Number Density

Different missions will encounter different ambient plasma parameters, which are characterized by the n_e and T_e. The integrals in equations (A8), (A10) and (A11) are not a function of n_e which is independent of E. Dividing the current densities by n_e we can plot them versus T_e to aid scientist and engineers in the probe or spacecraft charging design process. The following equation shows the electron current density divided by the number density:

$$j_e/n_e = -q_e\frac{2\pi}{m_e^2}\int_{E^*}^\infty EdE\int_0^\pi sin\theta d\theta\;\; f'(E) \quad \text{(A12)}$$

where $f'(E)=f(E)/n_e$. Similarly, the SE current density and BSE current densities can be divided by n_e :

$$j_{SE}/n_e = -q_e\frac{2\pi}{m_e^2}\int_0^\infty dE_{se}\int_{E^*}^\infty EdE\int_0^\pi sin\theta d\theta\;\delta(E,\theta)\;g_{se}(E_{se},E)\;\; f'(E) \quad \text{(A13)}$$

and

$$j_{BSE}/n_e = -q_e\frac{2\pi}{m_e^2}\int_0^\infty dE_{bse}\int_{E^*}^\infty EdE\int_0^\pi sin\theta d\theta\;\eta(E,\theta)\;g_{bse}(E_{bse},E)f'(E) \quad \text{(A14)}$$

H. NASCAP Fit Parameters

This section shows the NASCAP parameter fits for all samples. Table A-I shows the SE yield parameter fits. Table AII shows the BSE parameter fits.

TABLE A I
NASCAP SEY FIT PARAMETERS

	δ_{max}	E_{max} (keV)	b_1 (Å)	n_1	b_2 (Å)	n_2
W Un.	1.81	0.276	1.21	0.577	1	1.79
W 1200°C	1.83	0.266	0.787	0.368	1	1.58
Nb-C103 Un.	1.81	0.269	1.16	0.584	1	1.78
Nb-C103 1200°C	1.97	0.252	0.867	0.46	1	1.71
TiN Un.	2.3	0.236	0.807	0.416	1	1.83
TiN 180°C	2.35	0.227	0.728	0.378	1	1.78
Ta-W 10% Un.	2.35	0.24	0.912	0.546	1	1.71
Ta-W 1200°C	2.31	0.247	0.733	0.42	1	1.57
Molly TZM Un.	2.19	0.216	1.13	0.84	1	1.81
Molly TZM 1200°C	2.22	0.229	0.744	0.485	1	1.63
Elgiloy Un.	1.96	0.253	0.66	0.487	1	1.69
Elgiloy 800°C	2.09	0.314	1.19	0.411	1	1.78
DAG-213 180°C	1.97	0.19	2.03	0.99	1	1.95

TABLE A II
NASCAP BSEY FIT PARAMETERS

Sample	$\bar{Z}$	Z_{eff}	η_0	$\left[\frac{\eta_0^R-\eta_0^N}{\eta_0^N}\right]$*
W Un.	74	10.5±1.5	0.155±0.016	
W 1200°C	74	16.4±1.8	0.210±0.015	***35%***
Nb-C103 Un.	44.1	8.9±1.3	0.137±0.015	
Nb-C103 1200°C	44.1	11.0±1.7	0.160±0.018	17%
TiN Un.	14.5	5.2±0.8	0.087±0.012	
TiN 180°C	14.5	5.7±0.7	0.096±0.010	10%
Ta-W 10% Un.	73.1	16.4±2.3	0.201±0.019	
Ta-W 1200°C	73.1	15.0±1.4	0.198±0.012	2%
Molly TZM Un.	41.8	6.2±0.8	0.102±0.011	
Molly TZM 1200°C	41.8	9.1±1.0	0.14±0.012	***37%***
Elgiloy Un.	27.3	8.9±1.0	0.137±0.012	
Elgiloy 800°C	27.3	8.0±1.0	0.126±0.012	-8%
DAG-213 180°C	4.1	3.5±0.8	0.058±0.014	

* Values greater than uncertainties in italics

ACKNOWLEDGMENT

M.F.D. would like to thank Dr. Wang for useful discussions of secondary emission process in spacecraft charging.

REFERENCES

[1] J. Christensen, "Electron Yield Measurements of High-Yield, Low-Conductivity Dielectric Materials," J. R. Dennison, F. Edwards, and D. M. Riffe, Eds., ed: ProQuest Dissertations Publishing, 2017.

[2] G. Wilson, A. Starley, and J. R. Dennison, "Electron Range Computational Tool for Arbitrary Materials Over a Wide Energy Range," presented at the 15th Spacecraft Charging Tech. Conf., Kobe, Japan, 2018.

[3] A. S. G. Wilson, L. Phillipps and J. R. Dennison, "A Predictive Range Expression: Applications and Limitations," *IEEE Trans. on Plasma Sci.,* vol. TBD, no. TBD, p. TBD, 2019.

[4] H. B. Michaelson, "Work Functions of the Elements," *Journal of Applied Physics,* vol. 21, no. 6, pp. 536-540, 1950.

[5] E. C. Whipple, "Potential of Surfaces in Space," *Report on Progress of Physics,* vol. 44, pp. 1197-1250, March 1981.

[6] S. E. DeForest, "Electrostatic Potentials Developed by ATS-5," *Photon and Particle Interactions with Surfaces in Space, ed. R*

Grard, Proceedings of the 6th Eslab Symposium, Noordwijk, The Nedetherlands, pp. 263-267, 1972.

[7] R. Olsen, "Observation of Differential Charging Effects on ATS-6," *Journal of Geophysical Research,* vol. 86, no. A8, pp. 6809-6819, August 1 1983.

[8] R. Olsen, "A threshold effect for spacecraft charging," *Journal of Geophysical Research,* vol. 88, pp. 493-499, 1983.

[9] S. T. Lai, "The Role of Surface Condition in the Yields of Secondary Electrons, Backscattered Electrons, and Photoelectrons From Spacecraft," *Plasma Science, IEEE Transactions on,* vol. 41, no. 12, pp. 3492-3497, 2013.

[10] S. T. Lai and M. F. Tautz, "Aspects of Spacecraft Charging in Sunlight," *IEEE Transactions on Plasma Science,* vol. 34, no. 5, pp. 2053-2061, 2006.

[11] D. A. McPherson, D. P. Cauffman, and W. R. Schober, "Spacecraft Charging at High Altitudes: SCATHA Satellite Program," *Journal of Spacecraft and Rockets,* vol. 12, no. 10, pp. 621-626, 1975.

[12] E. C. Whipple, Jr., "The equilibrium electric potential of a body in the upper atmosphere and in interplanetary space - NASA-TM-X-55368," ed: Sponsoring Organization: NASA Goddard Space Flight Center, 1965.

[13] S. T. Lai, "Spacecraft charging: incoming and outgoing electrons," *CERN Yellow Report,* vol. 2, pp. 165-168, 2013.

[14] I. Katz, M. J. Mandell, G. A. Jongeward, and M. S. Gussenhoven, "The Importance of Accurate Secondary Electron Yields in Modeling Spacecraft Charging," ed. La Jolla, C. A.: S-Cubed, 1986.

[15] J. R. Dennison, R. C. Hoffmann, and J. Abbott, "Triggering Threshold Spacecraft Charging with Changes in Electron Emission from Materials," in *45th AIAA Aerospace Sciences Meeting and Exhibit*(Aerospace Sciences Meetings: American Institute of Aeronautics and Astronautics, 2007.

[16] H. B. Garrett, "The charging of spacecraft surfaces," *Reviews of Geophysics,* vol. 19, no. 4, pp. 577-616, 1981.

[17] A. G. Rubin, H. B. Garrett, and A. H. Wendel, "Spacecraft Charging on ATS-5," M. A. Air Force Geophysics Lab Hanscom Afb, Ed., ed, 1980.

[18] L. K. Sarno-Smith *et al.*, "Spacecraft surface charging within geosynchronous orbit observed by the Van Allen Probes," *Space Weather,* vol. 14, no. 2, pp. 151-164, 2016.

[19] J. Reagan, R. Nightingale, E. Gaines, R. Meyerott, and W. Imhof, "Role of energetic particles in charging/discharging of spacecraft dielectrics," J. Reagan, Ed., ed, 1981.

[20] E. G. Mullen, M. S. Gussenhoven, D. A. Hardy, T. A. Aggson, B. G. Ledley, and E. Whipple, "SCATHA survey of high-level spacecraft charging in sunlight," *Journal of Geophysical Research: Space Physics,* vol. 91, no. A2, pp. 1474-1490, 1986.

[21] M. J. Mandell, *NASCAP programmer's reference manual [microform] / M.J. Mandell, P.P. Stannard, and I. Katz.* Washington, DC] : [Springfield, Va.: [Washington, DC] : National Aeronautics and Space Administration ; [Springfield, Va. : National Technical Information Service, distributor, 1993], 1993.

[22] B. Thiebault, Mateo Velez, J-C. Forest, J., Sarrailh, P., "SPIS 5.1 User Manual," 2013.

[23] J. W. Bonnell *et al.*, "The Electric Field Instrument (EFI) for THEMIS," *Space Science Reviews,* vol. 141, no. 1, pp. 303-341, 2008.

[24] J. R. Wygant *et al.*, "The Electric Field and Waves Instruments on the Radiation Belt Storm Probes Mission," *Space Science Reviews,* vol. 179, no. 1, pp. 183-220, 2013.

[25] D. A. Gurnett *et al.*, "The Cassini Radio and Plasma Wave Investigation," *Space Science Reviews,* vol. 114, no. 1, pp. 395-463, 2004.

[26] L. Andersson *et al.*, "The Langmuir Probe and Waves (LPW) Instrument for MAVEN," *Space Science Reviews,* vol. 195, no. 1, pp. 173-198, 2015.

[27] R. B. Torbert *et al.*, "The FIELDS Instrument Suite on MMS: Scientific Objectives, Measurements, and Data Products," *Space Science Reviews,* vol. 199, no. 1-4, p. 105, 2016.

[28] A. Vaivads, A. I. Eriksson, M. André, L. G. Blomberg, J. E. Wahlund, and S. D. Bale, "Low-frequency electric field and density fluctuation measurements on Solar Orbiter," *Advances in Space Research,* vol. 39, no. 9, pp. 1502-1509, 2007.

[29] S. D. Bale *et al.*, "The FIELDS Instrument Suite for Solar Probe Plus," *Space Science Reviews,* vol. 204, no. 1-4, p. 49, 2016.

[30] R. E. Davies and J. R. Dennison, "Evolution of Secondary Electron Emission Characteristics of Spacecraft Surfaces," *Journal of Spacecraft and Rockets,* vol. 34, no. 4, pp. 571-574, 1997.

[31] J. R. Dennison, "Dynamic Interplay Between Spacecraft Charging, Space Environment Interactions, and Evolving Materials," *Plasma Science, IEEE Transactions on,* vol. 43, no. 9, pp. 2933-2940, 2015.

[32] W. Y. Chang, J. Dennison, N. Nickles, and R. E. Davies, "Utah State University Ground-based Test Facility for Study of Electronic Properties of Spacecraft Materials," presented at the Proceedings of the 6th Spacecraft Charging Technology Conference, Air Force Research Laboratory Science Center, Hanscom Air Force Base, MA, 2000.

[33] R. C. Hoffmann, "Electron-induced electron yields of uncharged insulating materials," 2010.

[34] O. Hachenberg and W. Brauer, "Secondary Electron Emission from Solids," in *Advances in Electronics and Electron Physics*, vol. 11, L. Marton and C. Marton, Eds.: Academic Press, 1959, pp. 413-499.

[35] M. S. Chung and T. E. Everhart, "Simple calculation of energy distribution of low-energy secondary electrons emitted from metals under electron bombardment," *Journal of Applied Physics,* vol. 45, no. 2, pp. 707-709, 1974.

[36] J. R. Dennison, J. Christensen, J. Dekany, C. Thomson, N. Nickles, Robert E. Davies, Mohamed Belhaj, Kazuhiro Toyoda, Arifur R. Khan, Kazutaka Kawasaki, Shunsuke Inoue, Isabel Montero, María E. Dávila and Leandro Olano, "Absolute Electron Emission Calibration: Round Robin Tests of Au and Polyimide," presented at the Proceedings of the 14th Spacecraft Charging Technology Conference, Noordwijk, Netherlands, Space Research and Technology Centre of the European Space Agency (ESA/ESTEC), , 2016.

[37] E. Brodu, "Thermal radiative properties and behavior of refractory metals, highly textured metallic coatings and pyrolytic boron nitride on C/C composite for the Solar Probe Plus mission," Ecole doctorale Energie Environment, Universite de Perpignan, Perpignan, 2014.

[38] D. Hastings and H. Garrett, *Spacecraft-Environment Interactions* (Cambridge atmospheric and space science series). New York: Cambridge University Press, 1996.

[39] N. Nickles, "The role of bandgap in the secondary electron emission of small bandgap semiconductors: Studies of graphitic carbon," J. R. Dennison, Ed., ed: ProQuest Dissertations Publishing, 2002.

[40] J. Wang, M. Pu Wang, J. C. M. Belhaj, and J. C. M. Velez, "Modeling Facility Effects on Secondary Electron Emission Experiment," *Plasma Science, IEEE Transactions on,* vol. 40, no. 10, pp. 2773-2780, 2012.

[41] M. Robertson, G. Wilson and JR Dennison, "Electron Yield of a Carbon-composite Nanodielectric," presented at the American Physical Society Four Corners Meeting, Colorado State University, Fort Collins, CO, 2017.

[42] G. Wilson, M. Robertson, J. Lee, and J. R. Dennison, "Electron Yield Measurements of Multilayer Conductive Materials," 2018.

[43] I. Langmuir, "The Effect of Space Charge and Residual Gases on Thermionic Currents in High Vacuum," *Physical Review,* vol. 2, no. 6, pp. 450-486, 1913.

[44] V. S. Fomenko, *Handbook of Thermionic Properties*. New York: Plenum Press Data Division, 1956.

[45] M. Diaz-Aguado, Bonnell, J. W., Bale, S.D., Rezvani, S.J., Koshmak, K., Giglia, A., Nannarone, S., Gruntman, M. , "Experimental Investigation of Total Photoemission Yield from New Satellite Surface Materials," *Accepted by the AIAA Journal of Spacecraft and Rockets, June 2018,* 2018.

[46] A. J. Ahearn, "The Emission of Secondary Electrons from Tungsten," *Physical Review,* vol. 38, no. 10, pp. 1858-1870, 1931.

[47] J. A. Reimer, R. W. Vaughan, and J. C. Knights, "Proton Magnetic Resonance Spectra of Plasma-Deposited Amorphous Si: H Films," *Physical Review Letters,* vol. 44, no. 3, pp. 193-196, 1980.

[48] R. L. Petry, "Secondary Electron Emission from Tungsten, Copper and Gold," *Physical Review,* vol. 28, no. 2, pp. 362-366, 1926.

[49] H. E. Krefft, "Critical primary velocities in the secondary electron emission of tungsten," *Journal of the Franklin Institute,* vol. 204, no. 4, pp. 537-539, 1927.

[50] N. R. Whetten, "Cleavage in High Vacuums of Alkali Halide Single Crystals—Secondary Electron Emission," *Journal of Applied Physics,* vol. 35, no. 11, pp. 3279-3282, 1964.

[51] P. Lundgreen and J. R. Dennison, "An analysis of Variations in Published Secondary Electron Yield Measurements of Copper,"

presented at the Four Corner Section Meeting of the American Physical Societry, Salt Lake City, UT, Fall 2018, 2016.
[52] E. J. Sternglass, "Backscattering of Kilovolt Electrons from Solids," *Physical Review,* vol. 95, no. 2, pp. 345-358, 07/15/ 1954.
[53] L. McDonnell, B. D. Powell, and D. P. Woodruff, "Temperature dependent peaks in secondary electron emission spectra," *Surface Science,* vol. 40, no. 3, pp. 669-682, 1973.
[54] R. Warnecke, "Secondary Emission of Pure Metals," *Journal de Physique,* vol. 6, pp. 269-280, 1936.
[55] S. Michizono, Y. Saito, Y. Suharyanto, S. Yamano, and S. Kobayashi, "Secondary electron emission of sapphire and anti-multipactor coatings at high temperature," *Applied Surface Science,* vol. 235, no. 1, pp. 227-230, 2004.
[56] M. M. Donegan, J. L. Sample, J. R. Dennison, and R. Hoffmann, "Spacecraft Coating-Induced Charging: Materials and Modeling Study of Environmental Extremes," *Journal of Spacecraft and Rockets,* vol. 47, no. 1, pp. 134-146, 2010.
[57] G. F. Dionne, "Origin of secondary-electron-emission yield-curve parameters," *Journal of Applied Physics,* vol. 46, no. 8, pp. 3347-3351, 1975.
[58] J. C. Phil Lundgreen, and JR Dennison, "Comparison of Models for Materials Parameters Used in Spacecraft Charging Codes," *IEEE Trans. on Plasma Sci.,* vol. TBD, p. TBD, 2019.
[59] A. J. Sims, "Electrostatic Charging of Spacecraft in Geosynchronous Orbit," F. Defence Research Agency, Ed., ed, 1992.
[60] S. M. L. Prokopenko and J. G. LaFroamboise, "High-Voltage Differential Charging of Geostationary Spacecraft," *Journal of Geophysical Research,* vol. 85, no. A8, pp. 4125-4131, 1980.
[61] E. M. Baroody, "A theory of secondary electron emission from metals," *Physical Review,* vol. 78, no. 6, pp. 780-787, 1950.
[62] N. Balcon, D. Payan, M. Belhaj, T. Tondu, and V. Inguimbert, "Secondary Electron Emission on Space Materials: Evaluation of the Total Secondary Electron Yield From Surface Potential Measurements," *Plasma Science, IEEE Transactions on,* vol. 40, no. 2, pp. 282-290, 2012.

Millan F. Diaz-Aguado (M'2018) received the B.S. and M.S. degree in aerospace engineering from University of Texas at Austin, TX, USA. He is currently pursuing the Ph.D. degree in astronautical engineering on the topic of spacecraft charging at University of Southern California (USC), CA, USA.

From 2007 to 2011, he was an Aerospace Engineer working as a contractor at NASA Ames Research Center, where he helped developed small astrobiology CubeSats and thermally designed the IRIS bus. From 2011 to 2016 he worked at Space Sciences Laboratories thermally designing instruments for Van Allen Probes, MAVEN and Parker Solar Probe. He is currently working at SRI International as a research engineer.

John W. Bonnell is a Project Physicist at the Berkeley Space Sciences Laboratory (SSL). He received his Ph.D. in Electrical Engineering from Cornell University in 1996. After three years of postdoctoral work at Cornell and Los Alamos National Laboratory, he joined UC Berkeley in 1999.

Bonnell is interested in experimental space plasma physics and the electrodynamics of momentum and energy transport and exchange in terrestrial and heliospheric plasmas. In particular, he focuses on the design and construction of electric field instrumentation; the design and use of multi-sensor and multi-point analysis of electric and magnetic field structures; auroral electrodynamics; and the observation and analysis of solar wind turbulence. Bonnell is a hardware lead for the electric field instrumentation and science Co-I on the NASA THEMIS/ARTEMIS, Van Allen Probes, and Parker Solar Probe missions, and PI or Co-I on several ongoing NASA sounding rocket campaigns, including GREECE, TRICE-2, and VIPER.

Stuart D. Bale is a Professor of Physics at the University of California, Berkeley. He is also the Director of the Berkeley Space Sciences Laboratory (SSL). He received his PhD in Physics from the University of Minnesota in 1994. After three years of postdoctoral work at Queen Mary College, University of London, he joined UC Berkeley. He has held visiting positions at the Observatoire de Paris, Meudon (Univ. Paris VII) and the University of Sydney. He is the recipient of the 2003 US Presidential Early Career Award for Scientists and Engineers (PECASE) and is a Fellow of the Royal Astronomical Society (UK) and a Fellow of the American Physical Society.

Bale is interested in experimental plasma astrophysics and particle energization in astrophysical and heliospheric plasmas. In particular, he uses satellite-borne experiments to make in situ observations of magnetic reconnection, collisionless shocks, and radio emission and nonlinear/turbulent plasma processes. He also has interests in solar and low frequency radio astronomy, plasma wave and electric field instrumentation and antenna design and signal processing techniques. Bale is the NASA Principal Investigator for experiments on the Wind, STEREO, and Parker Solar Probe missions.

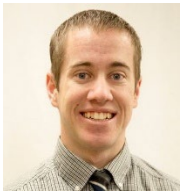

Justin Christensen received MS and BS degrees in physics at Utah State University in Logan, UT in 2017 and 2014, respectively. He worked with the Materials Physics Group for four years, focusing on electron emission and cathodoluminescent studies related to spacecraft charging. He is currently a Laboratory Support Technologist with the Physics Based Microsystems Group at Sandia National Laboratories

Phil Lundgreen is currently a graduate student at Utah State University in Logan, UT pursuing an MS in physics. He received a BS degree in physics from USU in 2014. He has worked with the Materials Physics Group for three years on electron transport measurements, electrostatic discharge analysis, electron emission evaluation, and development of a spacecraft materials charging database

Jordan Lee received his B.S. degree in Psychology from Southern Utah University, Cedar City, UT in 2012, and a B.S. degree in Physics from Utah State University (USU), Logan, UT in 2018. Currently he is an instrumentation specialist for the Material Physics Group at USU, collecting and analyzing data relevant to electron emission and permittivity for use in space-like conditions.

JR Dennison received the B.S. degree in physics from Appalachian State University, Boone, NC, in 1980, and the M.S. and Ph.D. degrees in physics from Virginia Tech, Blacksburg, in 1983 and 1985, respectively. He was a Research Associate with the University of Missouri—Columbia before moving to Utah State University (USU), Logan, in 1988. He is currently a Professor of physics at USU, where he leads the Materials Physics Group. He has worked in the area of electron scattering for his entire career and has focused on the electron emission and conductivity of materials related to spacecraft charging for the last two decades. IEEE member.

Justin Dekany is currently a graduate student at Utah State University in Logan, UT pursuing an MS in physics. He received a BS degree in physics from USU in 2010. He has worked with the Materials Physics Group for six years on electron transport measurements, electrostatic discharge tests, electron emission measurements, and luminescence studies related to spacecraft charging

Brian Wood received his M.S. and B.S. in physics at Utah State University in Logan, UT in 2011 and 2015 respectively, where he studied nanotechnology and fabrication associated with carbon nanotubes. Currently, he has been a researcher with the Materials Physics Group for 2 years studying electron transport, electron emission, and radiation effects testing related to spacecraft charging

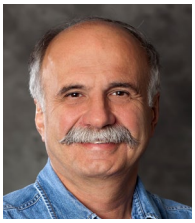

Mike Gruntman is a Professor of Astronautics at the University of Southern California (USC) and the founder of the USC Astronautics Program. He served the founding chairman of the Department of Astronautical Engineering from 2004-2007 and chairs it from 2016-2019. His research interests include astronautics, space physics, instrumentation and sensors, rocketry and propulsion, satellite design and technologies, space debris, space education, and history of rocketry, spacecraft, and missile defense. Mike authored and co-authored 300 scholarly publications, including 4 books.